The Astrophysical Journal, 748:123 (25pp), 2012 April 1 doi:10.1088/0004-637X/748/2/123
© 2012. The American Astronomical Society. All rights reserved. Printed in the U.S.A.

THE *HERSCHEL* REFERENCE SURVEY: DUST IN EARLY-TYPE GALAXIES AND ACROSS THE HUBBLE SEQUENCE*

M. W. L. Smith[1], H. L. Gomez[1], S. A. Eales[1], L. Ciesla[2], A. Boselli[2], L. Cortese[3], G. J. Bendo[4], M. Baes[5], S. Bianchi[6], M. Clemens[7], D. L. Clements[8], A. R. Cooray[9], J. I. Davies[1], I. de Looze[5], S. di Serego Alighieri[6], J. Fritz[5], G. Gavazzi[10], W. K. Gear[1], S. Madden[11], E. Mentuch[12], P. Panuzzo[11], M. Pohlen[1], L. Spinoglio[13], J. Verstappen[5], C. Vlahakis[14,15], C. D. Wilson[12], and E. M. Xilouris[16]

[1] School of Physics & Astronomy, Cardiff University, The Parade, Cardiff CF24 3AA, UK; matthew.smith@astro.cf.ac.uk
[2] Laboratoire d'Astrophysique de Marseille, UMR6110 CNRS, 38 rue F. Joliot-Curie, F-13388 Marseille, France
[3] European Southern Observatory, Karl Schwarschild Str. 2, 85748 Garching bei Muenchen, Germany
[4] School of Physics and Astronomy, University of Manchester, Oxford Road, Manchester M13 9PL, UK
[5] Sterrenkundig Observatorium, Universiteit Gent, Krijgslaan 281 S9, B-9000 Gent, Belgium
[6] INAF-Osservatorio Astrofisico di Arcetri, Largo E. Fermi 5, 50125 Firenze, Italy
[7] INAF-Osservatorio Astronomico di Padova, Vicolo dell'Osservatorio 5, 35122 Padova, Italy
[8] Astrophysics Group, Imperial College, Blackett Laboratory, Prince Consort Road, London SW7 2AZ, UK
[9] Center for Cosmology and the Department of Physics & Astronomy, University of California, Irvine, CA 92697, USA
[10] Universita' di Milano-Bicocca, Piazza della Scienza 3, 20126 Milano, Italy
[11] CEA, Laboratoire AIM, Irfu/SAp, Orme des Merisiers, F-91191 Gif-sur-Yvette, France
[12] Department of Physics & Astronomy, McMaster University, Hamilton, Ontario L8S 4M1, Canada
[13] Istituto di Fisica dello Spazio Interplanetario, INAF, via del Fosso del Cavaliere 100, 00133 Roma, Italy
[14] Joint ALMA Office, Alonso de Cordova 3107, Vitacura, Santiago, Chile
[15] Departamento de Astronomia, Universidad de Chile, Casilla 36-D, Santiago, Chile
[16] Institute of Astronomy and Astrophysics, National Observatory of Athens, I. Metaxa and Vas. Pavlou, P. Penteli, 15236 Athens, Greece
Received 2011 December 2; accepted 2012 January 11; published 2012 March 15

ABSTRACT

We present *Herschel* observations of 62 early-type galaxies (ETGs), including 39 galaxies morphologically classified as S0+S0a and 23 galaxies classified as ellipticals using SPIRE at 250, 350, and 500 μm as part of the volume-limited *Herschel* Reference Survey (HRS). We detect dust emission in 24% of the ellipticals and 62% of the S0s. The mean temperature of the dust is $\langle T_d \rangle = 23.9 \pm 0.8$ K, warmer than that found for late-type galaxies in the Virgo Cluster. The mean dust mass for the entire detected early-type sample is $\log M_d = 6.1 \pm 0.1\ M_\odot$ with a mean dust-to-stellar-mass ratio of $\log(M_d/M_*) = -4.3 \pm 0.1$. Including the non-detections, these parameters are $\log M_d = 5.6 \pm 0.1$ and $\log(M_d/M_*) = -5.1 \pm 0.1$, respectively. The average dust-to-stellar-mass ratio for the early-type sample is fifty times lower, with larger dispersion, than the spiral galaxies observed as part of the HRS, and there is an order-of-magnitude decline in M_d/M_* between the S0s and ellipticals. We use UV and optical photometry to show that virtually all the galaxies lie close to the red sequence yet the large number of detections of cool dust, the gas-to-dust ratios, and the ratios of far-infrared to radio emission all suggest that many ETGs contain a cool interstellar medium similar to that in late-type galaxies. We show that the sizes of the dust sources in S0s are much smaller than those in early-type spirals and the decrease in the dust-to-stellar-mass ratio from early-type spirals to S0s cannot simply be explained by an increase in the bulge-to-disk ratio. These results suggest that the disks in S0s contain much less dust (and presumably gas) than the disks of early-type spirals and this cannot be explained simply by current environmental effects, such as ram-pressure stripping. The wide range in the dust-to-stellar-mass ratio for ETGs and the lack of a correlation between dust mass and optical luminosity suggest that much of the dust in the ETGs detected by *Herschel* has been acquired as the result of interactions, although we show these are unlikely to have had a major effect on the stellar masses of the ETGs. The *Herschel* observations tentatively suggest that in the most massive systems, the mass of interstellar medium is unconnected to the evolution of the stellar populations in these galaxies.

Key words: galaxies: elliptical and lenticular, cD – galaxies: evolution – galaxies: ISM – submillimeter: galaxies

1. INTRODUCTION

In the standard theoretical view of galactic evolution, based on the hierarchical paradigm, galaxies may move both directions along the Hubble sequence during their evolution: ellipticals may form as the result of the merging of late-type galaxies (e.g., Cole et al. 2000; De Lucia et al. 2006); disks form as the result of the accretion of gas on to bulges (Cole et al. 2000). There are also plenty of environmental processes that might transform the morphology of a galaxy, just one example among many being ram-pressure stripping in clusters, which would move a galaxy toward the early-type sequence by removing the interstellar medium (ISM; e.g., Corbelli et al. 2011) and thus quenching star formation (Boselli & Gavazzi 2006).

The observational evidence that galaxy transformation is occurring is mixed, especially for galaxies at the current epoch. The fact that the morphology–density relation is not just the result of early-type galaxies (ETGs)—ellipticals and S0s—being more common in clusters, but extends over a wide range of environmental density, is evidence that galaxy transformation is not a significant process at the current epoch (Dressler 1980). However, there is also plenty of observational evidence that merging

* *Herschel* is an ESA space observatory with science instruments provided by European-led Principal Investigator consortia and with important participation from NASA.

is still important today. In particular, there is evidence of recent merging or accretion in nearby ellipticals, primarily from obscuration in the optical (Goudfrooij & de Jong 1995), where fossils of mergers in the form of dust ripples and dust lanes have been detected (Schweizer & Seitzer 1992). Furthermore, the discovery with the *Infrared Astronomical Satellite* (*IRAS*) of the ultraluminous infrared galaxies (ULIRGs), which are often late-stage mergers with optical profiles similar to the profiles of ellipticals (Wright et al. 1990), was persuasive evidence that ellipticals are still being formed by mergers at the current epoch. Nevertheless, it is not clear whether all the properties of the eventual merged systems would be the same as present-day ellipticals (Naab & Ostriker 2009), and many of the distinctive properties of ellipticals seem more naturally explained if ellipticals form in a relatively short early period in cosmic history (Peebles & Nusser 2010).

The properties of the ISM in ETGs potentially have something to tell us about the evolution of these systems. Since late-type galaxies are known to contain much more gas and dust than ETGs, any process that moves a galaxy along the Hubble sequence has to change simultaneously the morphology and the ISM of the galaxy. In this paper, we present *Herschel* observations of continuum emission from the dust in a sample of the most massive ETGs in the nearby universe, which we show is the most sensitive method currently available for estimating the mass of the cool ISM in these galaxies.

Although once thought to be devoid of a cool ISM, optical absorption studies suggested that more than 50% of ellipticals contain some dust (Goudfrooij et al. 1994; van Dokkum & Franx 1995; Tran et al. 2001; Ferrarese et al. 2006) and therefore molecular gas, though the mass of dust is uncertain from these works. In the last decade, previous far-infrared observations with *IRAS*, the *Infrared Space Observatory* (*ISO*), *Spitzer*, and *AKARI* have shown that dust in ETGs is rather common, with dust masses estimated at some 10–100 times larger than those derived from the optical extinction measurements (e.g., Bregman et al. 1998; Ferrari et al. 2002; Kennicutt et al. 2003; Pahre et al. 2004; Xilouris et al. 2004; Temi et al. 2004, 2007a; Panuzzo et al. 2007; Kaneda et al. 2008; Young et al. 2009). Although these observations have probed the peak of the spectral energy distributions (SEDs) of the brightest giant ellipticals and S0s, they are hampered by poor resolution and/or lack of long wavelength coverage.

Our current ideas about the life cycle of dust in ellipticals suggest that it may be possible for us to test the origin of the dust, particularly whether it is provided by internal (via stellar mass loss) or external processes (e.g., fueled by mergers). As long as dust is not introduced from elsewhere, we essentially have a stellar system in equilibrium: dust is produced in the atmospheres of evolved stars (Athey et al. 2002) and destroyed via sputtering in the hot gas (indeed, Bressan et al. 2006 detect silicate features in elliptical galaxies known to be produced in circumstellar envelopes). The dust life cycle in ellipticals may therefore be simpler than that in late types for the internal origin scenario (Tsai & Mathews 1996), and the mass of dust predicted to exist in the steady state through production in evolved stars and destruction through sputtering is approximately $10^5\,M_\odot$ (Forbes 1991; Goudfrooij & de Jong 1995).

An alternative origin for dust in ETGs is accreted material either due to a merger or from a tidally interacting companion: Centaurus A has long been known to harbor a dusty disk thought to be formed by a merger (recently revealed in the submillimeter (submm)—Leeuw et al. 2002; Auld et al. 2011; Parkin et al. 2011). Forbes (1991) and Temi et al. (2004, 2007a) found no correlation between the dust emission and optical starlight using *ISO* observations of massive ETGs, suggesting that the dust has an external rather than an internal origin. In 2010, Gomez et al. used *Herschel* observations of the elliptical galaxy M86 to reveal $10^6\,M_\odot$ of cold dust coincident with material stripped from the nearby spiral NGC 4438 (Cortese et al. 2010a). A similar process has been seen with the "displaced ISM" of the elliptical NGC 3077 (Walter et al. 2011).

The unprecedented resolution and sensitivity of the recently launched *Herschel Space Observatory* (Pilbratt et al. 2010), combined with the wavelength coverage of the instruments PACS (Poglitsch et al. 2010) and SPIRE (Griffin et al. 2010) from 70 to 500 μm, allow us to address long-standing issues such as the origin and quantity of dust in ETGs. *Herschel* provides us with an unbiased view of the interstellar dust (and therefore the interstellar medium); we are now sensitive to the *total* dust mass in galaxies rather than only to those galaxies which had enough warm dust to be detected by *IRAS* and *Spitzer* (e.g., Dunne et al. 2011). Here, we use observations from the guaranteed time project, the *Herschel* Reference Survey (HRS; Boselli et al. 2010b) of 62 ETGs including 23 ellipticals. The HRS is a study of dust in nearby galaxies, crucial for calibrating blind surveys of galaxies with *Herschel* at high redshifts, e.g., HerMES (Oliver et al. 2010) and *Herschel*-ATLAS (H-ATLAS; Eales et al. 2010).

Cortese et al. (2012, hereafter C12) recently used the HRS sample of ∼300 nearby galaxies to obtain dust scaling relations, finding that the dust is tightly coupled to the atomic mass and therefore to the cold ISM. C12 measured the dust-to-stellar-mass ratio of galaxies with different morphological types and environment, finding that the ETGs contain less dust mass per unit of stellar mass than the late-type galaxies. In this work, we further explore the dust properties of the ETGs in the HRS and measure more precisely the variation of dust content with Hubble type and the origin of this variation. In Section 2 we introduce the sample and describe the data reduction techniques. The results are given in Section 3 and are used to discuss our understanding of the dust content of early and late types in Section 4.1 and the link between dust and the hot interstellar medium in Section 4.2. We discuss the implications for the evolutionary history of ETGs in Section 5. The conclusions are presented in Section 6.

2. THE SAMPLE

The HRS is a volume-limited sample (15 Mpc $<$ d $<$ 25 Mpc) with *Herschel*/SPIRE of 322 galaxies selected by the *K*-band magnitude (a proxy for stellar mass). The ETGs in the HRS have $K \leqslant 8.7$, and so our sample consists of the ETGs in this volume of space with the highest stellar masses; contamination from Galactic cirrus is minimized due to the high galactic latitudes of the sample (see Boselli et al. 2010b for full details). The sample includes different morphological types with 260 late-type galaxies and, in the original catalog listed in Boselli et al. (2010b), 64 early types. However, after closer inspection of the optical images, we reclassified the galaxies NGC 4438 (HRS163), NGC 4457 (HRS173), NGC 4691 (HRS256), and NGC 5701 (HRS322) as late types (from S0/a to Sb). We changed two classifications in the other direction, with the Sb galaxies NGC 4179 (HRS90) and IC3510 (HRS202) reclassified to S0 and dwarf elliptical, respectively. The revised catalog therefore has 62 ETGs, 39 of which are designated S0+S0a galaxies and 23 are ellipticals (Table 1)

Table 1
The Sample

HRS	Other Name	R.A. (h m s)	Decl. (° ′ ″)	Type	D (Mpc)	$D(25)$ (′)	L_B ($L_\odot$)	L_K ($L_\odot$)	Membership
3	NGC 3226	10 23 27.01[r]	+19 53 54.7[r]	E2:pec;LINER;Sy3	16.7	3.16	10.12	10.59	Leo Cl.
7	NGC 3245	10 27 18.40[r]	+28 30 26.3[r]	SA(r)0:?;H II;LINER	18.8	3.24	10.08	10.47	Leo Cl.
14	NGC 3301	10 36 56.04	+21 52 55.7	(R')SB(rs)0/a	19.2	3.55	9.84	10.47	Leo Cl.
22	NGC 3414	10 51 16.19[r]	+27 58 30.2[r]	S0 pec;LINER	20.2	3.55	9.98	10.73	Leo Cl.
43	NGC 3608	11 16 58.96	+18 08 54.9	E2;LINER:	15.8	3.16	10.11	10.70	Leo Cl.
45	NGC 3619	11 19 21.51[r]	+57 45 28.3[r]	(R)SA(s)0+:	22.1	2.69	9.87	10.57	Ursa Major Cl.
46	NGC 3626	11 20 03.80[r]	+18 21 24.3[r]	(R)SA(rs)0+	21.3	2.69	10.12	10.70	Leo Cl.
49	NGC 3640	11 21 06.85	+03 14 05.4	E3	17.9	3.98	10.43	11.06	Leo Cl.
71	NGC 3945	11 53 13.61[r]	+60 40 32.3[r]	SB(rs)0+;LINER	18.0	5.25	10.01	11.06	Ursa Major Cl.
87	NGC 4124	12 08 09.64	+10 22 43.4	SA(r)0+	17.0	4.10	9.70	10.38	Virgo Out.
90	NGC 4179	12 12 52.11	+01 17 58.9	S0[a]	17.0	3.80	9.89	10.60	Virgo Out.
93	NGC 4203	12 15 05.06[r]	+33 11 50.2[r]	SAB0−:;LINER;Sy3	15.6	3.39	9.89	10.73	Coma I Cl.
101	NGC 4251	12 18 08.31	+28 10 31.1	SB0? sp	15.3	3.63	13.86	10.54	Coma I Cl.
105	NGC 4262	12 19 30.58	+14 52 39.8	SB(s)0−?	17.0	1.87	9.69	10.43	Virgo A
123	NGC 4324	12 23 06.18	+05 15 01.5	SA(r)0+	17.0	3.52	9.65	10.38	Virgo S Cl.
125	NGC 4339	12 23 34.94	+06 04 54.2	E0;Sy2	23.0	2.31	9.71	10.34	Virgo B
126	NGC 4340	12 23 35.31	+16 43 19.9	SB(r)0+	17.0	3.60	9.81	10.44	Virgo A
129	NGC 4350	12 23 57.81	+16 41 36.1	SA0;Abs. line	17.0	3.20	9.91	10.64	Virgo A
135	NGC 4365	12 24 28.23	+07 19 03.1	E3	23.0	8.73	10.34	11.26	Virgo B
137	NGC 4371	12 24 55.43	+11 42 15.4	SB(r)0+	17.0	5.10	9.92	10.68	Virgo A
138	NGC 4374, M84	12 25 03.78	+12 53 13.1	E1;LERG;Sy2	17.0	10.07	10.57	11.26	Virgo A
150	NGC 4406, M86	12 26 11.74	+12 56 46.4	S0(3)/E3	17.0	11.37	10.66	11.31	Virgo A
155	NGC 4417	12 26 50.62	+09 35 03.0	SB0: s	23.0	3.60	10.08	10.77	Virgo B
161	NGC 4429	12 27 26.56	+11 06 27.1	SA(r)0+;LINER;H II	17.0	8.12	10.23	11.06	Virgo A
162	NGC 4435	12 27 40.50[r]	+13 04 44.5[r]	SB(s)0;LINER;H II	17.0	2.92	10.05	10.83	Virgo A
166	NGC 4442	12 28 03.89	+09 48 13.0	SB(s)0	23.0	5.05	10.36	11.12	Virgo B
174	NGC 4459	12 29 00.04[r]	+13 58 42.2[r]	SA(r)0+;H II;LINER	17.0	3.36	10.07	10.91	Virgo A
175	NGC 4461	12 29 03.01	+13 11 01.5	SB(s)0+:	17.0	3.52	9.90	10.57	Virgo A
176	NGC 4469	12 29 28.03	+08 44 59.7	SB(s)0/a? sp	23.0	4.33	9.97	10.82	Virgo B
178	NGC 4472, M49	12 29 46.76	+08 00 01.7	E2/S0;Sy2	17.0	10.25	10.90	11.59	Virgo S Cl.
179	NGC 4473	12 29 48.87	+13 25 45.7	E5	17.0	4.04	10.15	10.90	Virgo A
180	NGC 4477	12 30 02.17	+13 38 11.2	SB(s)0:?;Sy2	17.0	3.60	10.12	13.77	Virgo A
181	NGC 4478	12 30 17.42	+12 19 42.8	E2	17.0	1.89	9.89	10.41	Virgo A
183	NGC 4486, M87	12 30 49.42	+12 23 28.0	E+0-1 pec;NLRG;Sy	17.0	11.00	10.85	11.43	Virgo A
186	NGC 4494	12 31 24.03	+25 46 29.9	E1-2;Sy	18.7	4.79	10.62	11.20	Coma I Cl.
200	NGC 4526	12 34 03.03[r]	+07 41 57.3[r]	SAB(s)0:	17.0	7.00	10.41	11.18	Virgo S Cl.
202	IC 3510	12 34 19.33	+11 04 17.7	dE[a]	17.0	1.10	8.70	9.20	Virgo A
209	NGC 4546	12 35 29.51	−03 47 35.5	SB(s)0−:	15.0	3.31	10.05	10.82	Virgo Out.
210	NGC 4550	12 35 30.61	+12 13 15.4	SB0: Sy,LINER	17.0	3.95	9.66	10.30	Virgo A
211	NGC 4552, M89	12 35 39.88	+12 33 21.7	E;LINER;H II;Sy2	17.0	7.23	10.29	11.06	Virgo A
214	NGC 4564	12 36 26.99	+11 26 21.5	E6	17.0	4.33	9.86	10.58	Virgo A
218	NGC 4570	12 36 53.40	+07 14 48.0	S0(7)/E7	17.0	3.52	9.96	10.70	Virgo S Cl.
219	NGC 4578	12 37 30.55	+09 33 18.4	SA(r)0:	17.0	3.77	9.71	10.41	Virgo E Cl.
231	NGC 4596	12 39 55.94	+10 10 33.9	SB(r)0+;LINER:	17.0	4.76	10.08	10.79	Virgo E Cl.
234	NGC 4608	12 41 13.29	+10 09 20.9	SB(r)0	17.0	4.30	9.83	10.51	Virgo E Cl.
235	NGC 4612	12 41 32.76	+07 18 53.2	(R)SAB0	17.0	2.16	9.82	10.35	Virgo S Cl.
236	NGC 4621, M59	12 42 02.32	+11 38 48.9	E5	17.0	7.67	10.32	11.05	Virgo E Cl.
240	NGC 4638	12 42 47.43	+11 26 32.9	S0-	17.0	2.01	9.82	10.49	Virgo E Cl.
241	NGC 4636	12 42 49.87	+02 41 16.0	E/S0/1;LINER;Sy3	17.0	9.63	10.51	11.18	Virgo S Cl.
243	NGC 4643	12 43 20.14	+01 58 42.1	SB(rs)0/a;LINER/H II	17.0	3.00	9.98	10.81	Virgo Out.
245	NGC 4649, M60	12 43 40.01	+11 33 09.4	E2	17.0	5.10	10.73	11.46	Virgo E Cl.
248	NGC 4660	12 44 31.97	+11 11 25.9	E5	17.0	1.89	9.70	10.47	Virgo E Cl.
250	NGC 4665	12 45 05.96	+03 03 20.5	SB(s)0/a	17.0	4.50	10.04	10.80	Virgo Out.
253	NGC 4684	12 47 17.52	−02 43 38.6	SB(r)0+;H II	21.3	2.88	9.82	10.42	Virgo Out.
258	NGC 4697	12 48 35.91	−05 48 03.1	E6;AGN	17.7	7.24	10.55	11.16	Virgo Out.
260	NGC 4710	12 49 38.93[r]	+15 09 59.1[r]	SA(r)0+? sp;H II	17.0	4.30	9.91	10.74	Virgo Out.
269	NGC 4754	12 52 17.56	+11 18 49.2	SB(r)0−:	17.0	5.03	10.05	10.81	Virgo E Cl.
272	NGC 4762	12 52 56.05	+11 13 50.9	SB(r)0 sp;LINER	17.0	8.70	10.21	10.85	Virgo E Cl.
286	NGC 4866	12 59 27.14	+14 10 15.8	SA(r)0+;LINER	17.0	6.00	9.84	10.60	Virgo Out.
296	NGC 5273	13 42 08.36[r]	+35 39 15.1[r]	SA(s)0;Sy1.5	15.2	2.75	9.54	10.21	Canes Ven. Spur
312	NGC 5576	14 21 03.68	+03 16 15.6	E3	21.2	3.55	10.16	10.89	Virgo-Libra Cl.
316	NGC 5638	14 29 40.39	+03 14 00.2	E1	23.9	2.69	10.09	10.72	Virgo-Libra Cl.

Notes. The columns are as follows. Column 1: the number of the source in the *Herschel* Reference Survey (Boselli et al. 2010b). Column 2: other common names for the galaxy. Columns 3 and 4: the right ascension and declination of the galaxy (J2000). This is taken from the NASA/IPAC Extragalactic Database (NED), except for positions with a superscript *r*, which are radio positions taken from Wrobel (1991) and Filho et al. (2006). Column 5: morphological type taken from Virgo Cluster Catalogue (Binggeli et al. 1985) or from our own classification. The AGN/Seyfert/LINER classifications were taken from Ho et al. (1997), Schmitt (2001), and Veron-Cetty & Veron (2006). Column 6: distance in Mpc. We assume all objects in Virgo, including those in the outskirts of Virgo, are at a distance of 17 Mpc, except for those in Cloud B, which we assume are at a distance of 23 Mpc. For the other galaxies we have calculated distances from the heliocentric velocity using a Hubble constant of 70 km s^{-1} Mpc^{-1}. Column 7: optical isophotal diameter (25 mag arcsec^{-2}). Column 8: total *K*-band luminosity measured using $K_{S_{\rm tot}}$ from 2MASS (Skrutskie et al. 2006). Column 9: cluster or cloud membership from Gavazzi & Boselli (1999) for Virgo, otherwise from Tully (1988) or Nolthenius (1993) wherever available, or, failing that, our own estimate.

[a] These sources were morphologically classified by hand using optical images.

though 5 of the latter set are morphologically classified as E/S0. The morphological classifications are taken from the Virgo Cluster Catalogue (Binggeli et al. 1985) or are our own if another was not available (Boselli et al. 2010b). The HRS contains galaxies from a range of environments, including isolated field galaxies, pairs, and galaxies in the heart of the Virgo Cluster.

The HRS observations were carried out with SPIRE in scan-map mode with a scan speed of 30 arcsec s^{-1}. We chose the size of our maps so that they would be at least as large as the optical disk of each galaxy, defined as the area of the galaxy within an optical isophote with a B-band brightness of 25 mag $arcsec^{-2}$ ($D(25)$; Boselli et al. 2010b). In practice, our maps were either 4×4, 8×8, or 12×12 $arcmin^2$, and in most cases are larger than $D(25)$. For each ETG, we made eight pairs of orthogonal scans, resulting in a 1σ instrumental noise in each pixel of 0.35, 0.20, and 0.11 MJy sr^{-1} for the 250, 350, and 500 μm, respectively (integration time of 1199 s, 3102 s, and 4948 s for each map size). We deliberately observed the ETGs in the HRS for at least twice as long as for the late-type galaxies (three pairs of orthogonal scans) because the former are known to contain much less dust on average.

There are a number of sources in the HRS which overlap with galaxies observed as part of the open-time key project the *Herschel* Virgo Cluster Survey (HeViCS; Davies et al. 2010, 2012), and thus the two surveys have a data-sharing agreement for these galaxies. Here we also include data of the duplicate 19 ETGs formally observed as part of HeViCS with both PACS and SPIRE. The SPIRE observations for HeViCS were made in parallel-scan-map mode with a scan speed of 60 arcsec s^{-1}. To cover the Virgo Cluster, four fields with size $4^\circ \times 4^\circ$ were observed with eight cross-scans (see Davies et al. 2010, 2012 for a complete description). Note that the dust content of all of the ETGs in the Virgo Cluster from HeViCS will be presented in a complementary paper (S. di Serego Alighieri et al., in preparation).

2.1. Data Reduction and Flux Extraction

The HRS and HeViCS SPIRE data were reduced using similar pipeline procedures. The SPIRE data were processed up to Level-1 with a custom script adapted from the official pipeline (*POF5_pipeline.py*, dated 2010 June 8) as provided by the SPIRE Instrument Control Centre (ICC).[17] Our custom Jython script was run in the *Herschel* Interactive Processing Environment (HIPE; Ott 2010) with the continuous integration build number: 4.0.1367. For both surveys we use an optimized deglitcher setting instead of applying the ICC default settings. For the HeViCS data the sigmaKappaDeglitcher module was used, while for the HRS we applied the waveletDeglitcher; this module was adjusted to mask the sample following a glitch. For the HRS, after the flux calibration was applied, an additional pass with the waveletDeglitcher was run, as this was found to significantly improve the glitch-removal process. Furthermore, we did not run the pipeline default temperature drift correction or the median baseline subtraction. Instead we use a custom method (BriGAdE; M. W. L. Smith et al., in preparation; see also L. Ciesla et al., in preparation) to remove the temperature drift and bring all bolometers to the same level.

Our final SPIRE maps were created using the naive mapper provided in the standard pipeline with pixel sizes of 6″, 8″, and 12″ at 250, 350, and 500 μm, respectively. The FWHM of the SPIRE beams for this pixel scale are 18.″2, 24.″5, and 36.″0 at 250, 350, and 500 μm, respectively (Swinyard et al. 2010). In addition, the 350 μm data are multiplied by 1.0067 to update our flux densities to the latest version 7 calibration product. The calibration uncertainty is a combination of the 5% error due to correlated errors between bands and the 2% random uncertainty; these values are added linearly instead of in quadrature.[18]

The *Herschel*/PACS 100 and 160 μm data taken as part of HeViCS were reduced using the standard pipeline (see Davies et al. 2012). In brief, we used a two-step deglitching process, first with the standard deglitcher and second using one based on sigma clipping. We masked bright sources and a high-pass filter was used to reduce $1/f$ noise. The orthogonal scans were combined and the naive mapper was used to create the final maps. Unlike Davies et al. (2012) we use images created using the full HeViCS data set with eight parallel-mode scans per tile. The FWHM beam sizes are approximately 9″ and 13″ with pixel sizes of 3.″2 and 6.″4 for the 100 and 160 μm bands, respectively.[19] Davies et al. (2012) measured differences in global flux densities of up to 20% between sets of cross-scans; we therefore choose this as a conservative error for our flux estimates as it dominates over other sources of uncertainty, e.g., the calibration.[20]

The 250 μm *Herschel*/SPIRE maps for the detected S0+S0a and all of the elliptical galaxies in our sample are shown in Figures 1 and 2. Most of the objects visible on the images are background galaxies, creating a potential problem for determining whether our targets are detected. Fortunately, these background galaxies are almost always unresolved, whereas virtually all our detections are extended. The full description of the flux extraction process and complete photometry information for all the HRS galaxies including upper limits on the non-detections are provided in L. Ciesla et al. (in preparation). The upper limits for the non-detections are estimated using circular apertures with sizes of $0.3 \times D_{25}$ for ellipticals and $0.8 \times D_{25}$ for S0s (chosen as a conservative limit based on the extent of 250 μm emission seen in the detected sample).

We tested the effect of using different definitions of the upper limit on the analysis in this paper. First, we used simply the statistical noise on the map, taking into account the instrumental noise and confusion to give $\sigma_{\rm rms}$. Second, we included the additional uncertainty in the photometry measurement due to the background level ($\sigma_{\rm sky}$; L. Ciesla et al., in preparation), which arises mainly from cirrus contamination. For this work, we use the photometry upper limit as in L. Ciesla et al. (in preparation), with $\sigma = 3(\sigma_{\rm rms} + \sigma_{\rm sky})$ which is the most conservative limit on the 250 μm flux for our sources. Note that all of the results in this paper are also valid if we use $3\sigma_{\rm rms}$ or $5\sigma_{\rm rms}$ (as a typical 3σ or 5σ detection limit).

For the HeViCS galaxies in our sample the PACS flux densities we used aperture photometry with suitable background regions selected around the source (the assumed uncertainty is outlined in Section 2.1). We present the PACS fluxes in Table 2.

[17] See "The SPIRE Analogue Signal Chain and Photometer Detector Data Processing Pipeline" (Griffin et al. 2008 or Dowell et al. 2010) for a more detailed description of the pipeline and a list of the individual modules.

[18] SPIRE Observer's Manual, 2011, *Herschel Space Observatory*, http://herschel.esac.esa.int/Docs/SPIRE/html/spire_om.html.

[19] PACS Photometer Calibration Document 2011, *Herschel Space Observatory*, http://herschel.esac.esa.int/twiki/pub/Public/PacsCalibrationWeb/pacs_bolo_fluxcal_report_v1.pdf.

[20] PACS Photometer Point Spread Function Document 2010, *Herschel Space Observatory*, http://herschel.esac.esa.int/twiki/pub/Public/PacsCalibrationWeb/bolopsfv1.01.pdf.

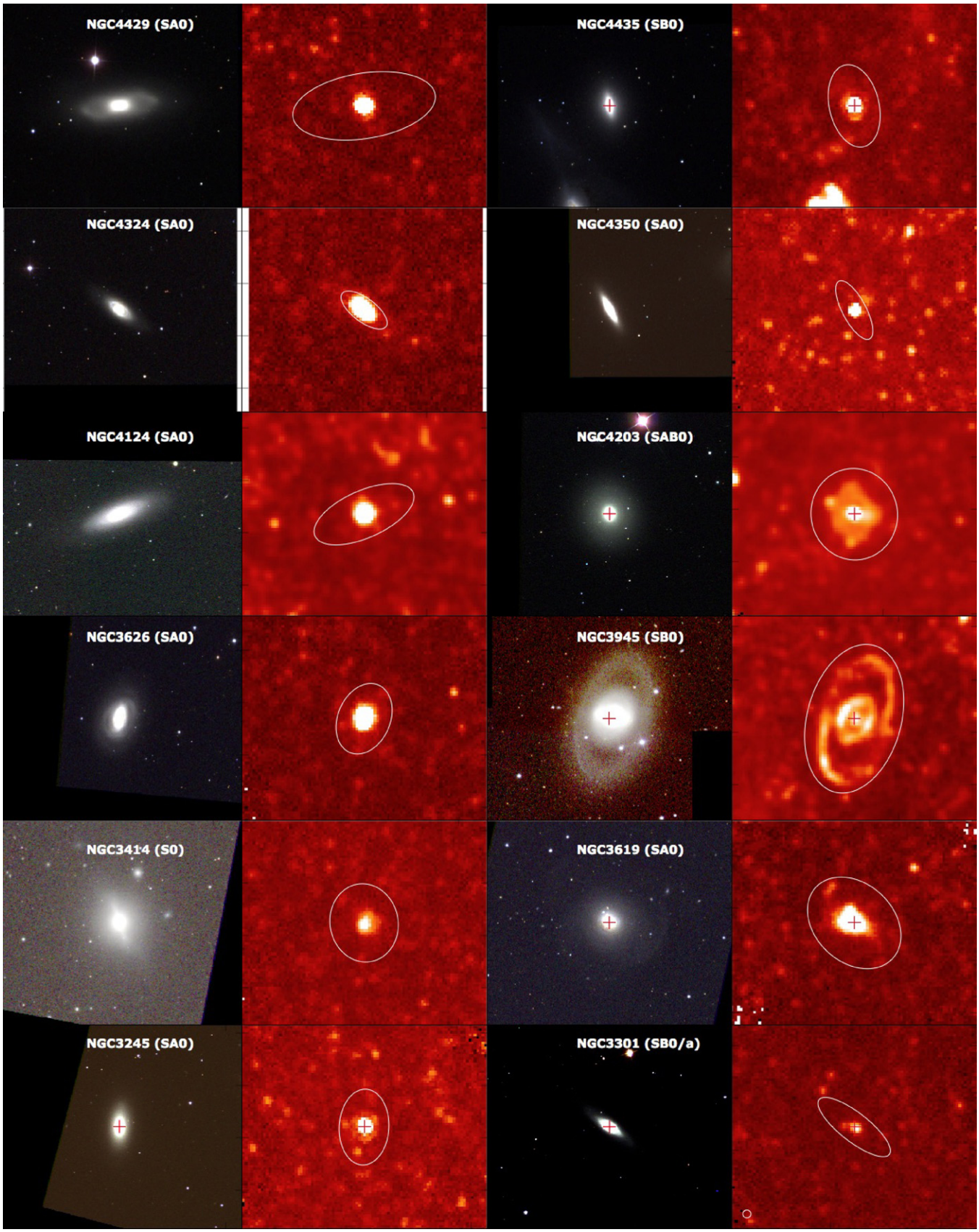

(a)

Figure 1. SDSS *gri* three-color maps and 250 μm *Herschel*/SPIRE maps of the 24 detected S0+S0a galaxies from the *Herschel* Reference Survey. North is up and east is left. The white aperture shows the elliptical optical *B*-band isophotal diameter ($D(25)$ at 25 mag arcsec^{-2}—Table 1). The region shown is $8.'4 \times 8.'4$. Red crosses show the location of the VLA FIRST radio detection. The 250 μm beam is shown in the corner of (a) NGC 3301 and (b) NGC 4469.

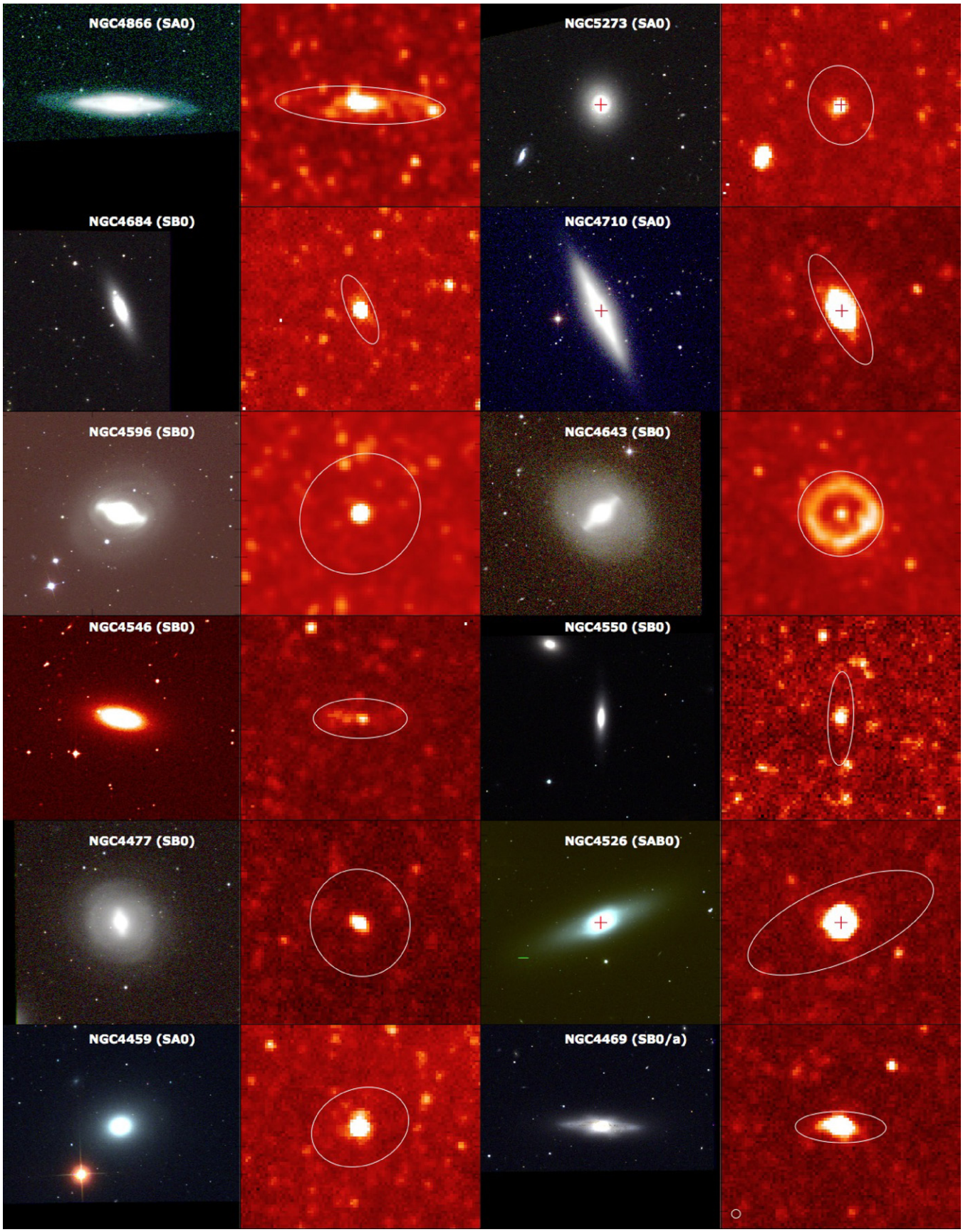

(b)

Figure 1. (Continued)

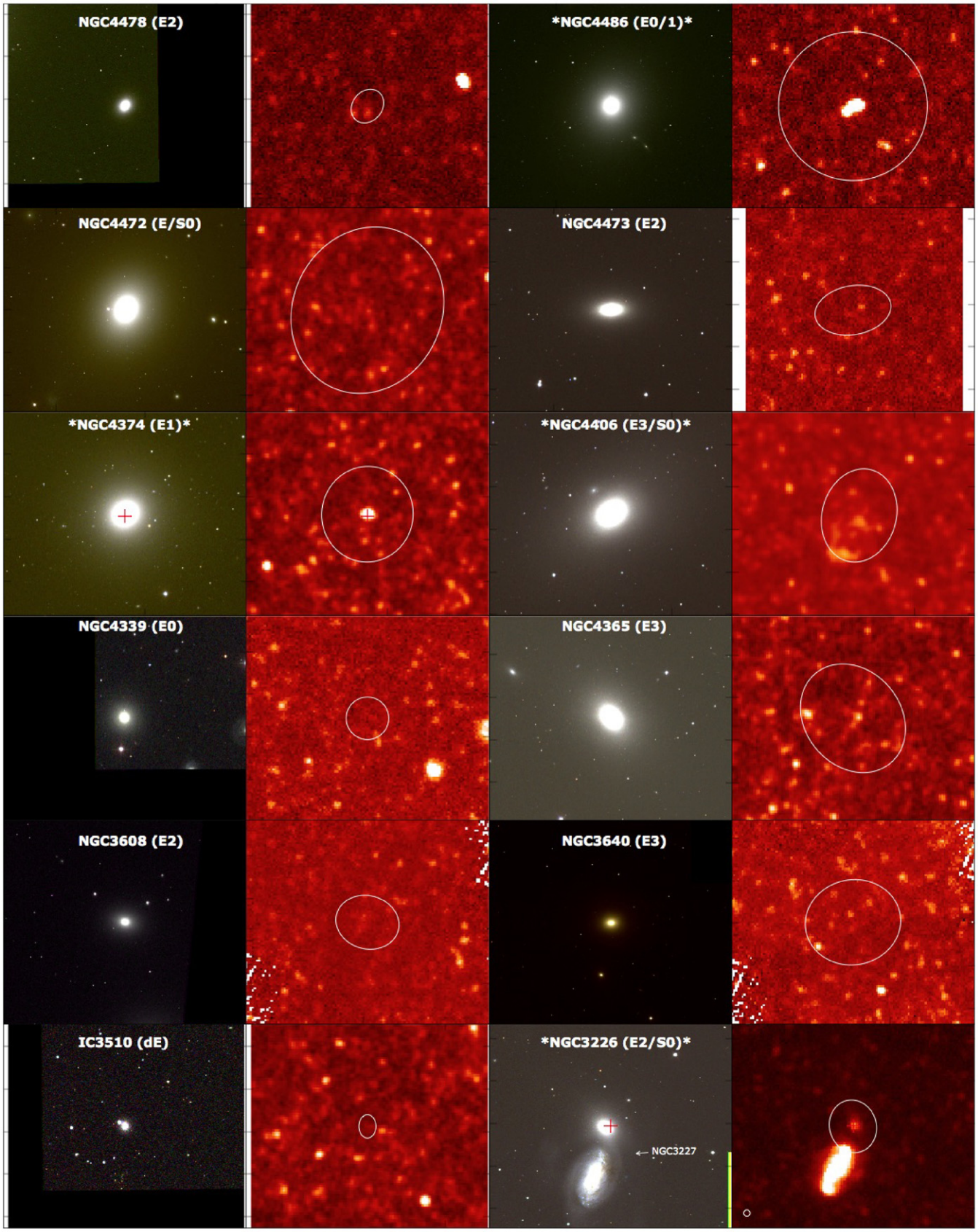

(a)

Figure 2. (a) SDSS *gri* three-color maps and 250 μm *Herschel*/SPIRE maps of the entire sample of 23 elliptical galaxies from the HRS and HeViCS programs (sources denoted with an (*) indicate that it has been detected by *Herschel*). North is up and east is left. The white aperture shows the optical *B*-band isophotal diameter ($D(25)$ at 25 mag arcsec^{-2}—Table 1). The boxes are $9\farcm6 \times 9\farcm6$. Red crosses show the location of the VLA FIRST radio detection and the 250 μm beam is shown in the corner of (a) NGC 3226 and (b) NGC 4552.

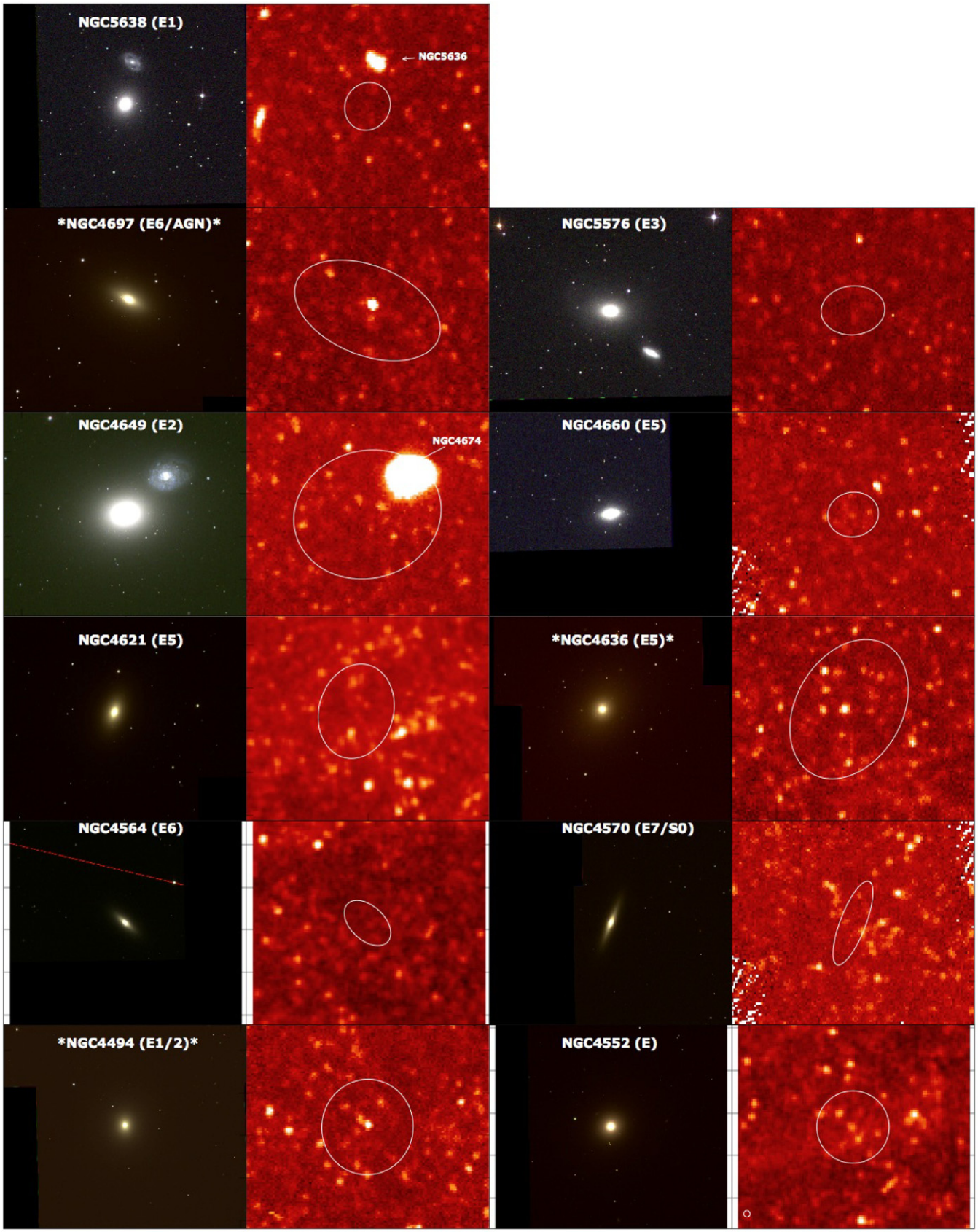

(b)

Figure 2. (Continued)

Table 2
Herschel/PACS and *IRAS* Fluxes for Detected Galaxies

HRS Name	F100 (Jy)	F160 (Jy)	F100 (Jy)	F60 (Jy)
7			3.97 ± 0.64	2.09 ± 0.28
14			0.92 ± 0.16	0.48 ± 0.07
22			0.56 ± 0.21	0.25 ± 0.04
45			1.83 ± 0.37	0.38 ± 0.06
71			1.36 ± 0.24	0.26 ± 0.04
87			1.75 ± 0.29	0.43 ± 0.07
93			2.16 ± 0.36	0.59 ± 0.08
101			...	0.12 ± 0.04
105	...	2.71 ± 0.542	0.39 ± 0.14	0.18 ± 0.04
123	1.80 ± 0.6	2.42 ± 0.48	1.99 ± 0.32	0.41 ± 0.07
126			0.37 ± 0.09	0.09 ± 0.03
129			1.09 ± 0.19	0.36 ± 0.06
138	0.78 ± 0.16	0.46 ± 0.09	1.16 ± 0.22	0.50 ± 0.07
150			0.33 ± 0.09	0.11 ± 0.04
161	4.74 ± 0.95	4.54 ± 0.91	5.15 ± 0.83	1.56 ± 0.21
162	4.48 ± 0.90	3.75 ± 0.75	...	...
174	4.59 ± 0.92	3.78 ± 0.75	4.82 ± 0.78	1.87 ± 0.25
176	3.33 ± 0.67	3.89 ± 0.78	3.40 ± 0.57	1.02 ± 0.14
180	0.94 ± 0.19	0.97 ± 0.19	1.41 ± 0.25	0.57 ± 0.09
183	0.38 ± 0.08	0.60 ± 0.12	0.41 ± 0.12	0.39 ± 0.07
186			...	0.19 ± 0.06
200	15.81 ± 3.16	15.53 ± 3.11	17.10 ± 2.74	5.56 ± 0.72
209			0.89 ± 0.26	0.26 ± 0.06
210	0.28 ± 0.06	0.27 ± 0.05	0.25 ± 0.10	0.14 ± 0.04
211			0.53 ± 0.10	0.16 ± 0.05
231			0.75 ± 0.13	0.40 ± 0.06
243			2.06 ± 0.34	0.62 ± 0.09
253			2.15 ± 0.36	1.27 ± 0.17
258			1.24 ± 0.21	0.46 ± 0.06
260			14.79 ± 2.37	5.73 ± 0.75
286			1.02 ± 0.23	0.15 ± 0.06
296			1.56 ± 0.28	0.90 ± 0.12
312			0.21 ± 0.28	0.09 ± 0.03
316			0.45 ± 0.14	...

Notes. The *ISO*, *Spitzer*, and *Herschel* photometry is presented in Temi et al. (2004), Bendo et al. (2011), and L. Ciesla et al. (in preparation), respectively. The columns are as follows. Column 1: the number of the source in the *Herschel* Reference Survey (Boselli et al. 2010b). Columns 2 and 3: *Herschel*/PACS fluxes at 100 and 160 μm. Columns 4 and 5: *IRAS* fluxes at 100 and 60 μm.

2.2. Data at Other Wavelengths

In addition to the *Herschel* data, we used 70–160 μm data from *Spitzer* (Kennicutt et al. 2003), reprocessed using the techniques described in Bendo et al. (2010b) and presented in Bendo et al. (2011). The calibration uncertainties were assumed to be 5% at 70 μm and 12% at 160 μm (Gordon et al. 2007; Stansberry et al. 2007). We use *IRAS* 60 and 100 μm measurements originally presented in Knapp et al. (1989) but modified in a private communication to NASA/IPAC Extragalactic Database (NED, Table 2). The calibration uncertainties for *IRAS* were assumed to be 13% at 60 μm and 16% at 100 μm (e.g., Verter & Rickard 1998). Four of our elliptical galaxies were also detected by *ISO* and we use the fluxes given in Temi et al. (2004).

Optical photometry for the sample was obtained from the Sloan Digital Sky Survey Data Release 7 (SDSS DR7; Abazajian et al. 2009) database. We estimate stellar masses for the sample from the *i*-band luminosities using the relationship between stellar mass and galaxy color for a Chabrier initial mass function (Zibetti et al. 2009). The full description of this method applied to the entire HRS sample can be found in Cortese et al. (2011) and C12. Near-UV (NUV) photometry is available from the *Galaxy Evolution Explorer* (*GALEX*; Martin et al. 2005) from the GR6 data release (see Boselli et al. 2011; Cortese et al. 2011).

X-ray luminosities for 38 of our sources were obtained from the catalogs of O'Sullivan et al. (2001) and Pellegrini (2010). A further 57 of our sources are included in the ATLAS^{3D} sample of ETGs (Cappellari et al. 2011a). ATLAS^{3D} includes molecular hydrogen masses estimated from the CO(1–0) intensity (I(CO); Young et al. 2011) with a conversion factor from H_2 to CO of $N(H_2)/I(CO) = 3 \times 10^{20}\,cm^2\,(K\,km\,s^{-1})^{-1}$ (e.g., Young & Scoville 1982). The CO data only exist for the central region of the galaxies (i.e., within 30″) and would be an underestimate of the total molecular gas if the real gas distribution is extended, though Young et al. find that there is no strong evidence for extended emission in any of the galaxies except for NGC 4649. Atomic H I masses and upper limits were obtained for 48 sources from the GOLDMINE database (Gavazzi et al. 2003), the ALFALFA survey (Haynes et al. 2011), or Noordermeer et al. (2005) and Springob et al. (2005). The CO and H I masses are presented in Table 4 . In all cases, these have been corrected to the distances assumed for the ETGs in this paper.

3. RESULTS

In Figure 1 we show the detected S0+S0a galaxies and all of the ellipticals in Figure 2; the sources show a variety of morphologies, from small blobs to spectacular ring structures. The difference in the appearance of the S0+S0a and ellipticals at 250 μm is very clear in these figures. The detected S0+S0a sources are brighter than their elliptical counterparts and the far-IR (FIR) emission is more extended within the $D(25)$ isophotes. In general, this appears to be a trend as we move along the Hubble sequence: an aperture of size $0.8 \times D(25)$ is sufficient to include the submm emission from the ETGs, yet L. Ciesla et al. (in preparation) require an aperture size of $1.4 \times D(25)$ to incorporate all the emission from the late-type galaxies. This effect was also noticed by Bendo et al. (2007) and Muñoz-Mateos et al. (2009).

The difference between late types and early types when viewed in the submm and optical wavebands is quite startling. For example, at optical wavelengths, the giant elliptical NGC 4649 (HRS245) is extremely bright compared to the smaller, fainter spiral galaxy to the northwest (NGC 4674). At 250 μm (Figure 2) however, the situation is reversed, with the spiral galaxy extremely bright in the FIR, but no sign of the elliptical. In Appendix A, we provide brief notes on the elliptical galaxies that are detected by *Herschel*.

3.1. Detection Rates

We detect 31 out of the 62 ETGs, including 24 S0+S0a galaxies (62%) and 7 ellipticals (30%, Table 3). We detect all three of the ETGs classified as "peculiar" (two ellipticals, M87 and NGC 3226, and one S0, NGC 3414). Our detection rates are higher than published in an *IRAS* study of ETGs (Bregman et al. 1998), which detected 12%–17%. Although the *IRAS* study excluded peculiar galaxies and active galactic nuclei (AGNs; with approximately half their sample at distances larger than the HRS), the small number of these sources in our sample suggests that the most likely explanation of the large difference in detection rates is that *Herschel* is more sensitive to cold dust than *IRAS*. This is supported by the higher mean

Table 3
The Number of Early-type and Elliptical Galaxies Detected with *Herschel*

Type	SPIRE Sample				X-Ray Sample						CO Sample					
	Observed		Detected 250		Observed		Detected X-ray		Detected 250		Observed		Detected CO		Detected 250	
	N	%	*N*	%	*N*	%	*N*	%	*N*	%	*N*	%	*N*	%	*N*	%
Total	62	100%	31	50%	38	61%	29	76%	15	52%	56	90%	16	28%	16	100%
E	21	34%	5	24%	20	53%	16	80%	4	25%	20	34%	0	0%	0	0%
S0	38	61%	23	63%	15	39%	11	77%	9	82%	35	63%	16	55%	16	100%
pec	3	5%	3	100%	3	8%	2	67%	2	100%	1	2%	0	0%	0	0%

	H I sample						Environment							
	Observed		Detected H I		Detected 250		Obs. Virgo		Det. Virgo		Obs. Not Virgo		Det. Not Virgo	
	N	%	*N*	%	*N*	%	*N*	%	*N*	%	*N*	%	*N*	%
Total	49	79%	17	35%	16	94%	47	76%	21	45%	15	24%	10	66%
E	15	31%	4	27%	4	100%	17	74%	5	29%	6	26%	2	33%
S0	34	69%	13	38%	12	92%	30	77%	16	53%	9	23%	8	88%
pec	0	0%	0	0%	0	0%	...	...	...	...	...	...	...	...

	$(b/a \leqslant 0.5)$								$(b/a > 0.5)$							
	Observed		Detected		Det. Virgo		Det. Not Virgo		Observed		Detected		Det. Virgo		Det. Not Virgo	
	N	%	*N*	%	*N*	%	*N*	%	*N*	%	*N*	%	*N*	%	*N*	%
S0	18	46%	12	67%	13/17	76%	1/1	100%	21	54%	12	57%	2/10	20%	9/11	82%
Barred	11	28%	6	55%	5/10	50%	1/1	100%	13	33%	6	46%	4/10	40%	2/3	67%

Notes. Top panel: the detection numbers for the 250 μm, X-ray, and CO samples in this work. Columns are as follows. Column 1: morphological type for the sample. Columns 2–5: *SPIRE*-detected sources including—Column 2: number of sources observed; Column 3: percentage of the observed sample which falls into the different types; Column 4: number of sources detected with SPIRE; Column 5: percentage detected with SPIRE compared to the observed sources in each morphological class. Columns 6–11: *X-ray sources* including—Columns 6 and 7: number of sources in our sample observed in X-ray from the literature and the percentage which falls into each morphological class (O'Sullivan & Ponman 2004; Pellegrini 2010); Columns 8 and 9: number and percentage of the observed X-ray sources which are detected in X-ray; Columns 10 and 11: number of sources detected in X-rays *and* detected with SPIRE. Columns 12–17: *CO sources* including—Columns 12 and 13: number of sources in our sample observed in CO from the literature and the percentage which falls into each morphological class (Young et al. 2011); Columns 14 and 15: number and percentage of the observed CO sources which are detected in CO; Columns 16 and 17: number of sources detected in CO *and* detected with SPIRE. Middle panel: the detection numbers for the H I and 250 μm sample, and for the entire 250 μm sample split by environment. Columns are as follows. Columns 2–7: H I *sources* including—Columns 2 and 3: number of sources in our sample observed in H I from the literature and the percentage which falls into each morphological class; Columns 4 and 5: number and percentage of the observed H I sources which are detected in H I; Columns 6 and 7: number of sources detected in H I *and* detected with SPIRE. Columns 8–15: *Environment:* the number and percentage in each subset defined as within the Virgo Cluster (Columns 8–11) and outside (Columns 12–15). Given the small numbers in the Virgo/non-Virgo samples, we do not separate the peculiar galaxies in this analysis. Bottom panel: the detection numbers for S0+S0a and barred S0 galaxies split into regimes depending on their axial ratios, where $b/a < 0.5$ and $b/a > 0.5$, indicating edge-on or face-on galaxies, respectively. Columns are as follows. Columns 2–9: *Edge-on galaxies* including–Columns 2 and 3: number and percentage of edge-on sources ($b/a < 0.5$); Columns 4 and 5: number and percentage of these sources which are detected with SPIRE. Columns 6 and 7: number of sources detected with SPIRE inside the Virgo Cluster and Columns 8 and 9 for those outside Virgo. Columns 10–17: *Face-on galaxies*—Columns 10 and 11: number and percentage of face-on sources ($b/a > 0.5$); Columns 12 and 13: number and percentage of those sources which are detected with SPIRE. Columns 14 and 15: number of sources detected with SPIRE inside the Virgo Cluster and Columns 16 and 17 for those outside Virgo.

dust temperature reported by Bregman et al. (1998). Temi et al. (2004) detected a higher fraction of ETGs (41% of ellipticals and 79% of S0s) with *ISO*, but their sample contains peculiar galaxies and giant ellipticals. The detection rates for the SPIRE and multiwavelength data for our sample are listed in Table 3; these rates are significantly[21] different for S0s and ellipticals at the 96% level. Our overall detection rate of 50% for the ETGs is higher than the 22% obtained by the ATLAS^{3D} CO study of 260 ETGs (Young et al. 2011), though the ATLAS^{3D} sample has a larger volume out to distances 46 Mpc (compared to 25 Mpc for the HRS). Comparing those HRS galaxies which are in both the ATLAS^{3D} and HRS (i.e., observed in both CO and dust continuum), the detection fraction in CO is a factor of two lower than at 250 μm. Similarly, for those galaxies with *Herschel* and H I observations, the detection fraction in H I is $\sim$1.5 times lower (Table 3). The *Herschel* observations of the continuum emission from the dust are therefore currently the most sensitive way of detecting the ISM in the HRS sample of ETGs.

[21] Using the two-sided Fisher's exact test, the equivalent of the χ^2 test but for small samples.

Given the small number of ellipticals that have been detected by *Herschel*, it is interesting to ask the question of what makes these special. Twenty of the ETGs in our sample are classified as having low-ionization narrow emission line regions (LINERs). The origin of LINER activity in ETGs can be ionizing photons from the old stellar population (e.g., di Serego Alighieri et al. 1990; Sarzi et al. 2010), heating by the hot ISM (Sparks et al. 1989) or AGN heating (e.g., González-Martín et al. 2009). At least 12 of the HRS sample have bright radio cores (Figure 1) suggesting AGN photoionization is important for at least 20% of the sample. For the most massive ellipticals, the hot ISM could be a significant photoionizing source; nine of the detected LINER sources in our sample have X-ray luminosities well above that expected from the discrete stellar population, i.e., $L_X/L_B \sim 10^{29.5}$ (O'Sullivan et al. 2001; Section 4.2) suggesting that a significant fraction of the LINER emission may originate from the hot ISM rather than an AGN source. Of the seven detected ellipticals, two are classified as LINERs, two as Seyfert galaxies, and a further two are unambiguously identified as containing a bright AGN (Ho et al. 1997; Schmitt 2001; Veron-Cetty & Veron 2010). Only one of the seven, NGC 4406

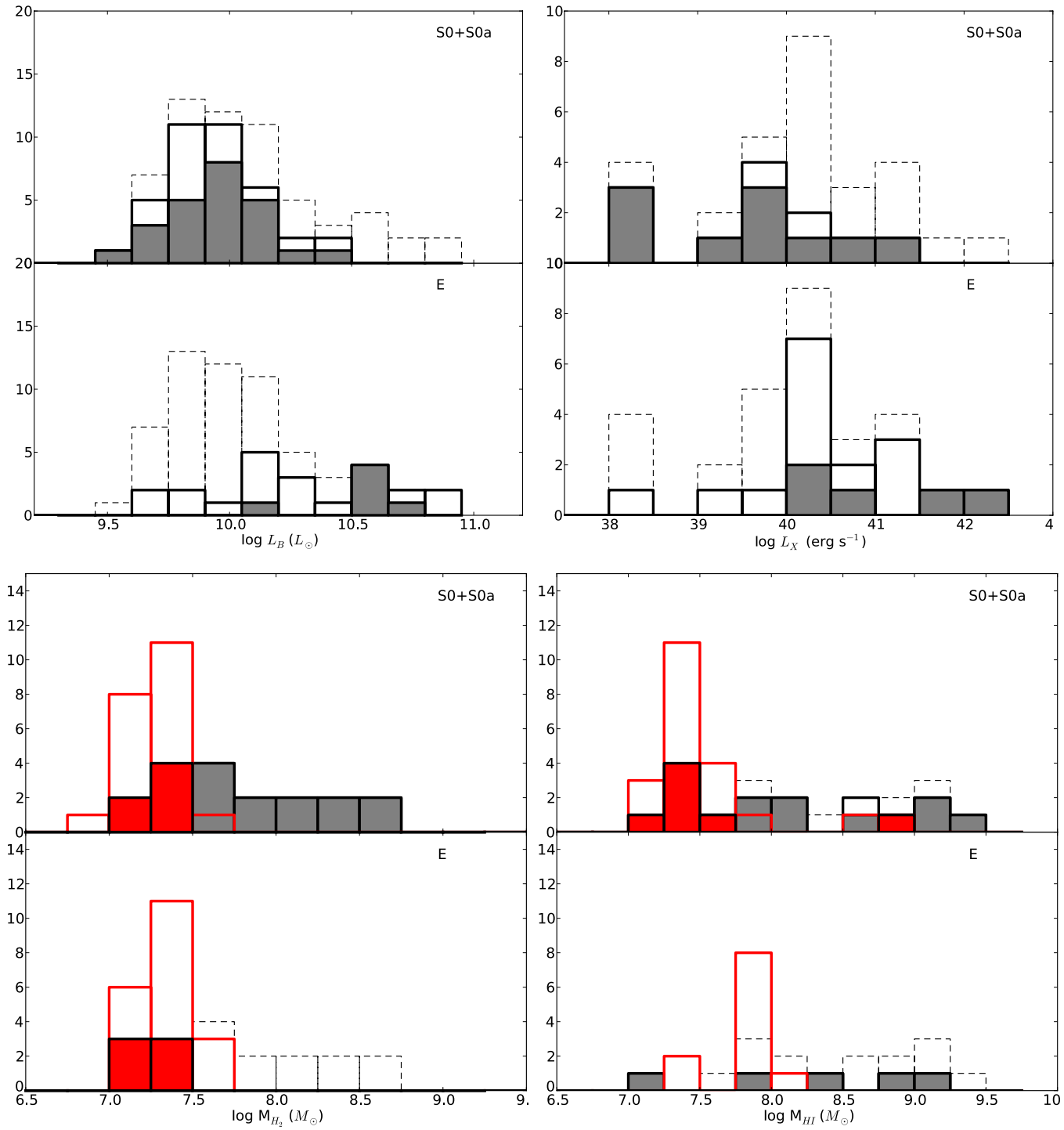

Figure 3. Top left: the range of *B*-band luminosities; top right: X-ray luminosities for the S0+S0a (top) and elliptical (bottom) galaxies. The outer dashed histogram shows the range of the whole sample (S0+S0a or E combined), the thick black unfilled histograms are the subsamples (S0+S0a and E separated out), and the detected sources are shaded gray. Bottom left: the molecular gas mass estimated from CO observations; bottom right: the atomic gas mass from H I. The red histograms show the upper limits on the gas mass obtained from the CO (H I), i.e., these are sources in our sample not detected either at 250 μm or CO (H I). The red shaded histogram shows the sources detected at 250 μm but *not* detected in CO (H I).

(HRS150) is a "pure" elliptical with no sign of an active nucleus, but this galaxy has acquired dust and atomic gas through a recent interaction (Gomez et al. 2010). Nine other "pure" ellipticals in our sample are not detected at 250 μm.

Another way to look at this question is to compare the properties of the detected and undetected sources in other wavebands. The distribution of the *B*-band luminosities for the sample is shown in Figure 3 along with the distributions of the detected sources. The figure shows that while there is no tendency for the detected S0 galaxies to be optically luminous, the detected elliptical galaxies are optically the most luminous ones.

Figure 3 shows a similar comparison for the X-ray luminosities. In this case, one might suspect that the galaxies with the highest X-ray luminosities from the hot halo are the least likely to be detected by *Herschel* because of sputtering. The figure

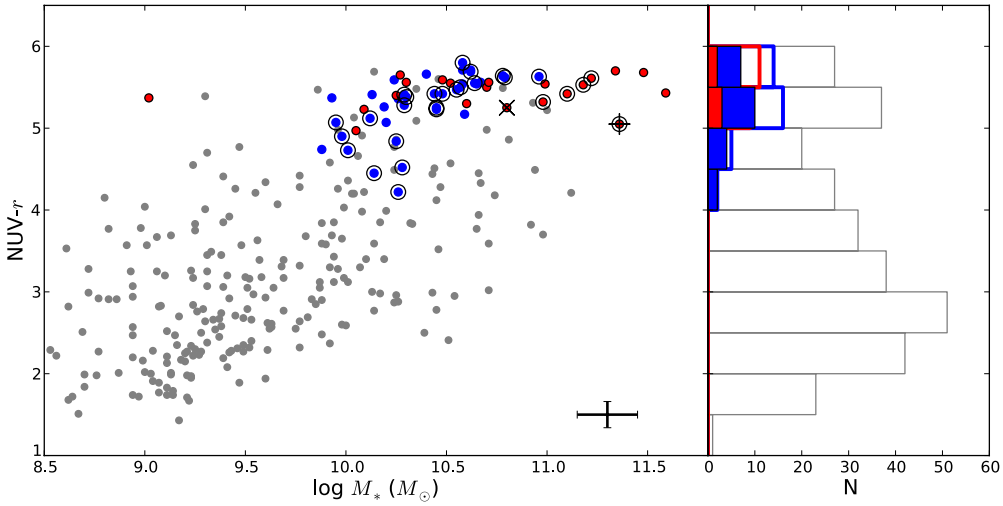

Figure 4. Left: the NUV − r color vs. the stellar mass of the HRS sample (L. Cortese et al., in preparation) including our morphologically classified spirals (gray; C12), S0+S0a (blue), and elliptical galaxies (red). The S0+S0a and elliptical galaxies detected with SPIRE are highlighted with the outer black circles. Note that the galaxy NGC 4486 is shown as detected in this plot but we do not see evidence for dust (above the synchrotron emission), NGC 4486 is highlighted with "+". The well-known galaxy with no evidence for star formation (NGC 4552) but with somewhat bluer NUV − r color than the average elliptical in our sample is highlighted with a "×". UV photometry exists for 87% of the ellipticals and 95% of the S0 sample. Right: the distribution of NUV − r colors for the observed samples split into spirals (gray), S0+S0a (blue), and ellipticals (red; unfilled histograms) including detections for the early types (shaded histograms).

shows that the elliptical galaxies detected at 250 μm tend to have higher X-ray luminosities so that elliptical galaxies more luminous in X-rays and optical (i.e., the most massive stellar systems) tend to be detected by *Herschel*. The detected S0 galaxies span a wide range of L_B and L_K, indicating that the stellar mass of these systems is not the critical factor for detection by *Herschel*.

In contrast to the X-rays, we find that galaxies containing large masses of cool gas are more likely to be detected by *Herschel* (Figure 3). CO observations of our sources taken from the ATLAS^{3D} survey (Young et al. 2011) suggest that 28% of our ETGs have molecular gas (Table 3), similar to the detection rate of 22% for the entire ATLAS^{3D} sample of 260 ETGs. Atomic hydrogen observations are available in the literature for 79% of our sample, although only 35% of these galaxies are detected.

We can also consider whether certain morphological types are more likely to be detected. Eighty percent of the undetected galaxies are morphologically classified as barred systems (NED; Table 1), which at first glance suggests that barred galaxies have less dust content than galaxies without a bar. However, we actually detect 50% of the barred sources from the HRS sample (Table 3), suggesting that the presence of a bar does not determine whether it is detected at 250 μm. Finally, we investigated whether the inclination angle might affect whether or not the galaxy was detected by *Herschel* using the measured axial ratios of the galaxies (minor axis/major axis—b/a). The detection rate for edge-on galaxies ($b/a < 0.5$) is 67% and for face-on galaxies ($b/a > 0.5$) is 57% though this is not statistically significant. Whether a galaxy has rings, bars, or high inclination angles therefore does not affect whether it is detected by *Herschel*.

One important effect on whether we detect ETGs with *Herschel* is environment. It has long been known that galaxies in dense environments are depleted in atomic gas, and recent *Herschel* observations have shown that this is also true of dust (Cortese et al. 2010b; C12). Gravitational interactions might also either remove or add gas and dust to a galaxy. We can do a rough comparison of the detection rates in different environments using the cluster or cloud membership listed in Table 1. Following C12, we split our sample into two sets: one set includes galaxies inside the Virgo Cluster and its outskirts ($N = 47$ galaxies) and the other set includes galaxies outside Virgo ($N = 15$). We detect 53% (16/30) of the S0s and 29% (5/17) of the ellipticals within the Virgo Cluster. Outside Virgo, we detect 89% (8/9) and 33% (2/6), respectively (Table 3). The detection rates are therefore lower for galaxies within the Virgo Cluster, but this is not at a significant level (see footnote 21).

3.2. Residual Star Formation?

We now discuss the NUV−r color for our sample; for star-forming galaxies, this is a useful measure of the specific star formation rate (SFR/M_*) since the NUV traces recent star formation and the r band is a proxy for stellar mass (e.g., Wyder et al. 2007). For Milky-Way-like extinction curves, the NUV is less affected by internal dust obscuration compared to the far-UV (FUV), but the NUV can also be affected by the presence of evolved hot stars (the UV-upturn, e.g., Greggio & Renzini 1990; Yi et al. 2011). Blue, star-forming galaxies occupy the region NUV − r < 3.5 (Kaviraj et al. 2007), the "blue cloud," with the red, passive ETGs found at NUV − r > 4.5 in the "red sequence." Although the color cut of NUV − r > 4.5 is often used to select galaxies on the red sequence, the most passive galaxies are significantly redder than this. Saintonge et al. (2011) have found that galaxies with NUV − r > 5 have very little molecular gas and Kaviraj et al. (2007), Schawinski et al. (2007), and Yi et al. (2005) have showed that quiescent non-star-forming ETGs occupy the region above the boundary NUV − r = 5.4.

Figure 4 shows the NUV−r color plotted against stellar mass for all the HRS galaxies taken from C12 and L. Cortese et al. (in preparation). Sources detected at 250 μm are highlighted with the outlined black circles. All but two galaxies in our early-type sample have NUV − r > 4.5 and most cluster around the line NUV − r = 5.5. If NUV − r < 5.4, the blue colors may be due to recent star formation but they may also be caused by the UV upturn. NGC 4552 is a famous example of this, with NUV − r ∼ 5.2, even though there is no residual star formation (Figure 4). Excluding NGC 4552, 12 out of 18 S0s

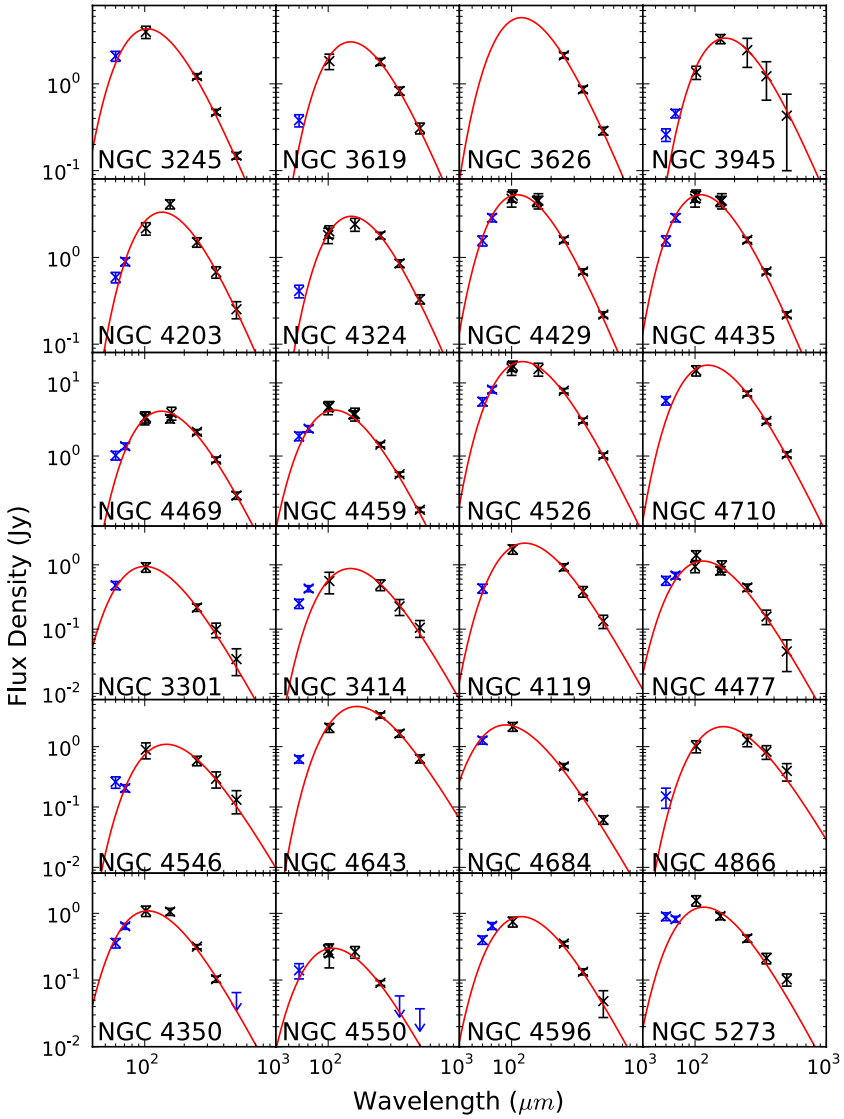

Figure 5. Spectral energy distributions of the 24 detected S0+S0a galaxies in our sample. The red solid line is the best-fit modified blackbody, blue points are fluxes used as upper limits, and black crosses are the photometry used for the cold dust component, including *Herschel*/SPIRE fluxes and PACS, *IRAS*, and *Spitzer* where available. Errors shown also include calibration errors (L. Ciesla et al., in preparation). The best-fit model parameters are provided in Table 4.

which lie below this boundary are detected with *Herschel*, and 2 out of 7 ellipticals. The two ellipticals are the AGN NGC 4486 (HRS138) and the (unusual) X-ray source NGC 4636 (HRS241); the NUV emission from these galaxies may be related to their central activity.

As we detect dust emission in almost half of the galaxies, the UV fluxes should be corrected for the dust attenuation since this will cause the galaxies to be redder in NUV $-$ r than they truly are. Given the complexity of disentangling the old and young stellar populations, we leave this for future work and, given the sensitivity of the NUV emission to internal dust extinction, we make no attempt to estimate the SFRs from the NUV $-$ r colors. Following Schawinski et al. (2007), we simply classify galaxies as quiescent where NUV $-$ r $>$ 5.4 and possibly undergoing recent star formation (RSF) where NUV $-$ r $<$ 5.4. In this case (including sources not detected with *GALEX* but excluding NGC 4486 and NGC 4552), ∼40% of our early-type sample is in the RSF group, including 30% of our ellipticals. This agrees with the fraction of SDSS ETGs found with RSF (Schawinski et al. 2007). Of course, our estimate may be biased in a number of ways, since we have not corrected for dust extinction and the colors of some of the galaxies in the RSF sample may be due to LINER-type activity or to the UV upturn.

The most interesting result, however, that can be seen in Figure 4 is the very large number of ETGs that lie on the red sequence but are still detected by *Herschel*. It is often assumed that the red sequence contains galaxies with virtually no current star formation and little interstellar gas, but the detection with *Herschel* of ≃50% of these galaxies clearly shows that they contain significant reservoirs of interstellar material agreeing with recent observations of CO in ETGs (Young et al. 2011).

3.3. Dust Masses and Temperatures

The global IR-submm SEDs of the detected S0+S0a and elliptical galaxies with available data from 60 to 500 μm are presented in Figures 5 and 6, respectively. NGC 4486 (M87) and NGC 4374 are both bright radio sources and their SEDs are well fitted by a power law at the longer FIR wavelengths. For the former, we find no evidence for dust emission above the power-law synchrotron component (in agreement with Baes et al. 2010). In NGC 4374, we do see a strong excess from dust

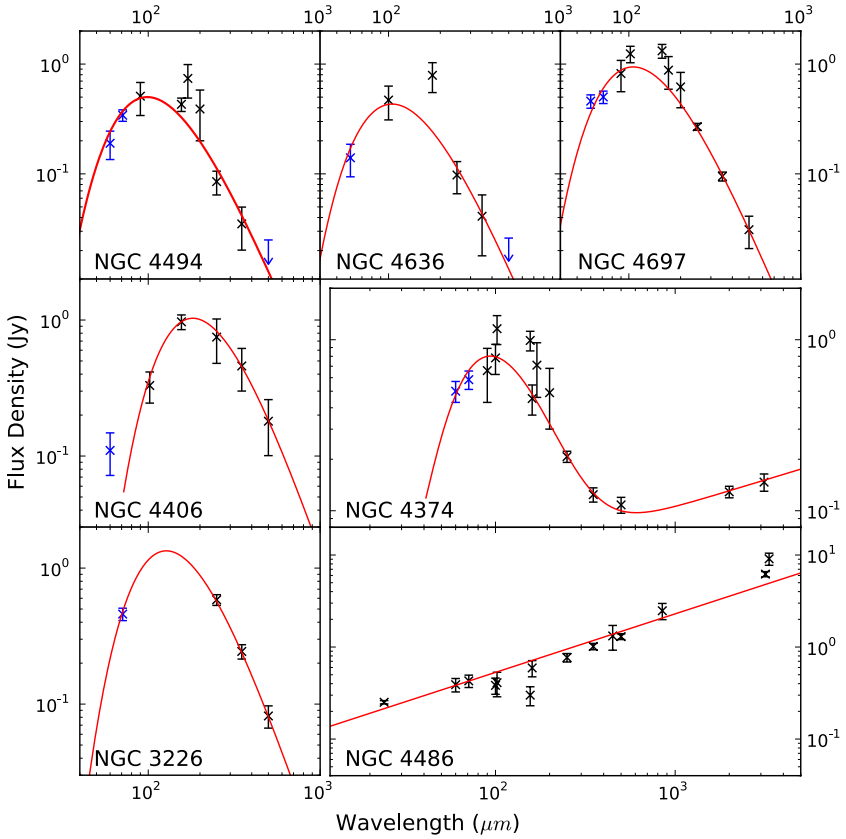

Figure 6. Spectral energy distributions of the seven detected ellipticals in our sample. Blue points are those fluxes used as upper limits and black crosses are the photometry used for the cold dust component, including *Herschel*/SPIRE and PACS, *IRAS*, *ISO*, and *Spitzer* where available. Radio fluxes are also shown by black points for NGC 4374 and NGC 4486 (M87). The red solid line is the best fit to the data and includes a modified (single temperature component) blackbody with $\beta = 2$ and a synchrotron component. Errors shown also include calibration errors (L. Ciesla et al., in preparation). These galaxies are discussed in more detail in Appendix A and the best-fit model parameters are listed in Table 4.

emission in the FIR. We fit the SEDs from 100 to 500 μm with a modified blackbody model, where

$$S_\nu = \frac{\kappa_\nu M_d B(\nu, T_d)}{D^2}, \quad (1)$$

M_d is the dust mass, T_d is the dust temperature, $B(\nu, T_d)$ is the Planck function, and D is the distance to the galaxy. κ_ν is the dust absorption coefficient described by a power law with dust emissivity index β, such that $\kappa_\nu \propto \nu^\beta$. For $\beta = 2$ (typical of Galactic interstellar dust grains), we use $\kappa_{350\mu m} = 0.19\,\mathrm{m^2\,kg^{-1}}$ (Draine 2003). Although κ is notoriously uncertain, virtually all of our analysis relies on κ being constant between galaxies rather than on its absolute value.

We assumed $D = 17$ Mpc for the Virgo Cluster (Gavazzi et al. 1999) and 23 Mpc for the Virgo B cloud; for all other galaxies, we estimated D from the recessional velocities using a Hubble constant of $H_o = 70\,\mathrm{km\,s^{-1}\,Mpc^{-1}}$.

We found the best-fit solution by minimizing the chi-squared (χ^2) difference between the model and the measured fluxes, involving the model with the filter transmission functions. To account for the uncertainties in the fluxes that are correlated between the SPIRE bands (5%), we used the full covariance matrix in the χ^2 calculation. The covariance matrix has diagonal elements with the total variance of each band and non-diagonal elements consisting of the covariance between bands from the correlated calibration uncertainties. We treated flux measurements at wavelengths $\leqslant 70\,\mu$m as upper limits for the cold dust emission as previous works (Smith et al. 2010; Bendo et al. 2010a) found that there is a significant contribution at these wavelengths from a warmer component of dust. We estimated uncertainties in the dust temperatures and masses using a bootstrap technique, in which we generated artificial sets of fluxes from the measured fluxes and errors, and then applied our fitting technique to each set of fluxes. The dust temperatures, and therefore dust masses, depend on the choice of β; $\beta = 1.5$ would yield slightly higher dust temperatures for the whole sample (Bendo et al. 2003) and therefore lower dust masses.

The SED for NGC 5273 (Figure 5) is the only source which appears to have an additional component present. Using the $\beta = 2$ one-temperature component described above provides an adequate fit to the photometry data if an additional synchrotron component is present. The SED is also adequately fit with a one-temperature dust component model with β as a free parameter, $\beta = 0.9$, or with a two-temperature dust component model. To fit the data with the latter model would require an additional component of $\sim$9 K dust, which would increase the dust mass by an order of magnitude. Both the $\beta = 2$ + synchrotron model and $\beta = 1$ model give a dust mass of $10^{5.45}\,M_\odot$, which is somewhat lower than the dust mass estimated using the $\beta = 2$ one-temperature dust component without synchrotron ($10^{5.65}\,M_\odot$) but within the errors (Table 4). As no millimeter data are available for this source, we cannot rule out synchrotron contamination, so in this analysis we have chosen to stick with the $\beta = 2$ one-component model to be consistent with the other sources.

We have estimated upper limits to the dust masses for the galaxies undetected by *Herschel* using the flux upper limit at 250 μm (including the noise on the image, an estimate

Table 4
SED Parameters and Gas Masses

HRS Name	Type	$\log L_{\rm FIR}$ ($L_\odot$)	T_d (K)	$\log M_d$ ($M_\odot$)	$\log M_{\rm H_2}$ ($M_\odot$)	$\log M_{\rm H\,I}$ ($M_\odot$)	Rotator
3	E	8.50	22.7 ± 1.29	5.96 ± 0.09	<7.13	...	F
7	S0	9.20	27.7 ± 1.5	6.14 ± 0.05	7.20	...	F
14	S0	8.57	29.0 ± 1.9	5.41 ± 0.12	<7.31	7.80[3]	F
22	S0	8.42	19.6 ± 2.0	6.26 ± 0.21	<7.02	...	S
43	E	<7.56	...	<4.88	<7.28	...	S
45	S0	9.04	19.6 ± 1.0	6.89 ± 0.07	8.11	8.89[3]	F
46	S0	9.38	24.4 ± 4.0	6.65 ± 0.17	8.29	9.02[3]	F
49	E	<7.88	...	<5.20	<7.25	...	F
71	S0	8.84	17.1 ± 1.1	7.05 ± 0.18	<7.28	...	F
87	S0	8.73	22.9 ± 1.0	6.17 ± 0.09	7.91	...	F
90	S0	<8.38	...	<5.70	<7.31	<7.68[1]	F
93	S0	8.81	21.4 ± 0.6	6.43 ± 0.07	7.63	9.44[4]	F
101	S0	<8.41	...	<5.73	<6.92	<7.39[1]	F
105	S0	<8.12	...	<5.44	<7.16	8.71[1]	F
123	S0	8.79	19.3 ± 0.6	6.68 ± 0.07	7.72	8.73[1]	F
125	E	<7.85	...	<5.17	<7.2	<7.84[1]	F
126	S0	<8.48	...	<5.80	...	<7.31[1]	F
129	S0	8.51	27.6 ± 0.6	5.47 ± 0.04	<7.27	<7.38[1]	F
135	E	<8.85	...	<6.17	<7.62	<8.18[1]	S
137	S0	<8.91	...	<6.23	<7.29	<7.38[1]	F
138	E	8.4	31.1 ± 1.0	5.05 ± 0.06	<7.16	8.96[1]	S
150	E	8.25	16.0 ± 1.1	6.63 ± 0.16	<7.4	7.95[2]	S
155	S0	<8.71	...	<6.03	<7.54	<7.64[1]	F
161	S0	9.18	26.3 ± 0.6	6.26 ± 0.04	8.05	<7.44[1]	F
162	S0	9.13	25.0 ± 1.2	6.34 ± 0.10	7.87	<7.31[1]	F
166	S0	<9.06	...	<6.38	<7.48	<7.64[1]	F
174	S0	9.11	26.4 ± 0.6	6.18 ± 0.03	8.29	<7.61[1]	F
175	S0	<8.29	...	<5.61	<7.23	<7.13[1]	F
176	S0	9.25	21.6 ± 0.7	6.83 ± 0.05	...	<7.64[1]	F
178	E	<8.45	...	<5.77	<7.25	<7.92[1]	S
179	E	<7.87	...	<5.19	<7.16	<7.92[1]	F
180	S0	8.49	25.2 ± 1.6	5.68 ± 0.11	7.54	<7.31[1]	F
181	E	<7.53	...	<4.85	<7.31	...	F
183	E	...	...	...	...	...	S
186	E	8.28	29.3 ± 1.3	5.08 ± 0.11	<7.35	8.26[1]	F
200	S0	9.7	23.9 ± 0.6	7.03 ± 0.04	8.62	7.13[1]	F
202	E	<7.61	...	<4.93	...	<7.37[1]	F
209	S	8.26	19.8 ± 0.8	6.08 ± 0.11	<7.05	...	F
210	S0	7.94	26.8 ± 1.8	4.97 ± 0.08	<7.32	8.79[1]	S
211	E	<8.35	...	<5.67	<7.36	<7.92[1]	S
214	E	<7.98	...	<5.30	<7.33	<7.79[1]	F
218	E	<8.35	...	<5.67	<7.47	<7.31[1]	F
219	S0	<8.41	...	<5.73	<7.24	<7.24[1]	F
231	S0	8.37	24.5 ± 1.3	5.64 ± 0.08	7.34	<7.19[1]	F
234	S0	<8.55	...	<5.87	<7.33	<7.44[1]	F
235	S0	<7.95	...	<5.27	<7.22	<7.38[1]	F
236	E	<8.44	...	<5.76	<7.24	<7.92[1]	F
240	S0	<8.20	...	<5.52	<7.30	<7.44[1]	F
241	E	8.11	27.6 ± 2.2	5.06 ± 0.19	<7.02	9.0[1]	S
243	S0	8.94	17.5 ± 0.7	7.08 ± 0.07	7.30	8.06[1]	F
245	E	<8.08	...	<5.40	<7.59	<7.92[1]	F
248	E	<7.53	...	<4.85	<7.30	<7.92[1]	F
250	S0	<9.14	...	<6.46	...	<8.66[1]	F
253	S0	9.1	32.2 ± 1.4	5.65 ± 0.06	7.63	8.22[3]	F
258	E	8.48	27.4 ± 0.7	5.46 ± 0.04	<7.25	...	F
260	S0	9.64	23.1 ± 1.2	7.06 ± 0.05	8.72	7.76[2]	F
269	S0	<8.95	...	<6.27	<7.23	<7.44[1]	F
272	S0	<9.16	...	<6.48	<7.23	<7.92[1]	F
286	S0	8.61	17.7 ± 1.2	6.73 ± 0.17	...	9.13[1]	F
296	S0	8.43	24.8 ± 2.6	5.65 ± 0.20	7.26	...	F
312	E	<8.19	...	<5.51	<7.46	...	S
316	E	<7.91	...	<5.23	<7.54	...	F

Notes. Column 1: HRS ID; Column 2: morphological classification; Columns 3 and 4: the FIR luminosity (of the cold dust component) and dust temperature; Columns 5: dust masses estimated using $\beta = 2$ and $\kappa_{350} = 0.19\,{\rm m^2\,kg^{-1}}$, 3 σ upper limits (L. Ciesla et al., in preparation) are quoted where the source is not detected using the mean dust temperature; Columns 6 and 7: molecular masses estimated from CO (Young et al. 2011) and H I masses (references below); Column 8: slow (S) or fast (F) rotator as defined by ATLAS[3D] (Emsellem et al. 2011).

References. (1) Gavazzi et al. 2003; (2) Haynes et al. 2011; (3) Springob et al. 2005; (4) Noordermeer et al. 2005.

[a] No SDSS data are available for HRS209 or HRS186.

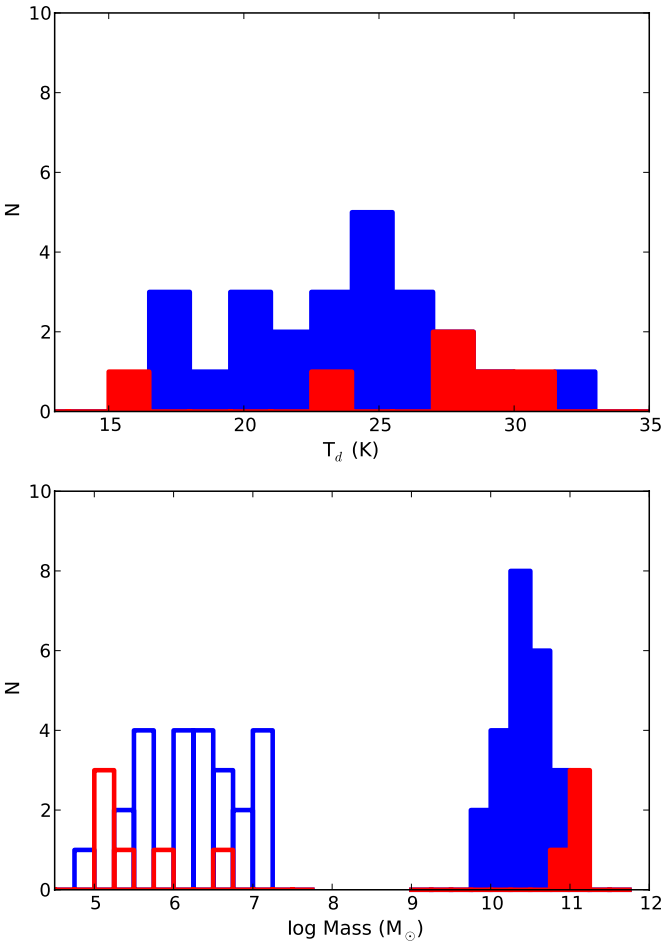

Figure 7. Top: histogram of the dust temperatures based on single modified blackbody fits; bottom: dust (left) and stellar masses (right shaded; L. Cortese et al., in preparation) for the detected ellipticals (red) and S0+S0a galaxies (blue)—see Table 4. The populations of the dust and stellar masses of the detected ellipticals and S0s are different with significance levels of $P > 97.9\%$ (M_d) and $P > 99.9\%$ (M_*) using a Mann–Whitney U-test.

of confusion noise and background variance in the map as described in L. Ciesla et al., in preparation) and the average temperature for the detected galaxies.

The dust masses and temperatures are presented in Table 4, and we show the range of dust temperatures, masses, and stellar masses for the S0+S0a and elliptical detected sample in Figure 7. These range from $M_d = 10^{5.0-7.1}\,M_\odot$ and 16–32 K with mean values of $10^{6.14}\,M_\odot$ and 24 K, respectively (Table 5). The stellar masses of these galaxies (C12) range from $10^{9.9-11.2}\,M_\odot$ with an average of $\langle \log M_*(M_\odot) \rangle = 10.89$; the average dust-to-stellar-mass ratio is $\log(M_d/M_*) = -4.33 \pm 0.14$. The M_d/M_* ratios are plotted in Figure 8 and clearly shows that, at the same stellar mass, there is a sharp fall in the dust-to-stellar-mass as we move from spirals to S0s (by roughly a factor of 10), and that this fall continues as we move from S0s to ellipticals (again, by a factor of 10). The two ellipticals with anomalously high values given their stellar mass are NGC 3226 (HRS3) and NGC 4406 (HRS150). Both galaxies show signs of a tidal interaction (see Appendix A), suggesting that the dust may have been acquired as the result of an interaction with a dust-rich galaxy.

4. DUST, STARS, AND GAS

In this section we compare the dust temperatures, masses, and dust-to-stellar ratios with other *Herschel* results of late-type

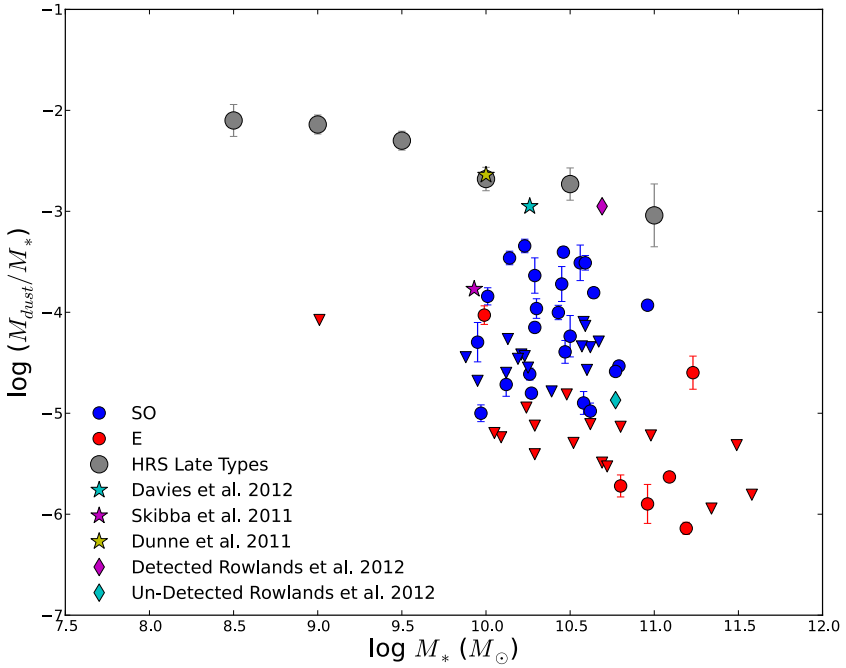

Figure 8. Dust-to-stellar-mass ratio vs. stellar mass. Blue points are the detected S0+S0a galaxies, with red points for the ellipticals. Upper limits on the dust mass are shown with triangles. The mean M_d/M_* for the HRS spirals in each stellar mass bin is shown with gray circles (see C12, their Figure 5) with error bars indicating the error on the mean. We also compare the mean M_d/M_* results of late types in HeViCS (blue star; Davies et al. 2012) and H-ATLAS (yellow star; Dunne et al. 2011), early types with H-ATLAS (Rowlands et al. 2012 for detected (purple diamond) and undetected (cyan diamond) early-type populations), and early types with KINGFISH (purple star; Skibba et al. 2011). The stellar masses are from L. Cortese et al. (in preparation).

and early-type galaxies. First, the temperatures for the HRS ETGs are generally higher than temperatures for the galaxies detected in blind submm surveys or in other samples of nearby galaxies (see Planck Collaboration 2011; Dunne et al. 2011) when corrected for different choices of β. We have tested whether the temperatures of ETGs are systematically higher than those of late types by comparing our dust temperatures with those of 71 Virgo galaxies in Davies et al. (2012) who used an identical method. We find that the temperatures of the early types are systematically higher (with $U = 1638$, $n_1 = 70$, $n_2 = 30$, and $P > 99.99\%$[22]), in agreement with the result that the ETGs in the HRS have warmer IR colors than late types (Boselli et al. 2010a; see also Bendo et al. 2003; Engelbracht et al. 2010).

In Figure 8, we compare the ratio of dust-to-stellar-mass for the HRS ETGs with the *Herschel* KINGFISH (Kennicutt et al. 2011) results based on 10 nearby early types (Skibba et al. 2011). They find warmer dust temperatures, with a mean of $\langle T_d \rangle = 30$ K (mostly due to the use of a lower emissivity index $\beta = 1.5$ compared to this work), and their sample has a lower average stellar mass compared to the HRS. Though their dust masses are similar, the dust-to-stellar-mass ratios are higher in KINGFISH than for the HRS. This may be a result of the different environments (a large fraction of the HRS galaxies are in a rich cluster) and/or the selection of the sample (KINGFISH ETGs may include unusual galaxies rather than the flux-selected ETGs in the HRS).

Rowlands et al. (2012) detected only $\simeq$5% of ETGs in a blind submm survey with *Herschel* at 250 μm, finding a median dust mass for their detected galaxies (in their lowest redshift bin) of $10^{7.8}\,M_\odot$ with average dust temperature consistent with the HRS ETG sample. Their dust mass is significantly higher than the dust masses of the HRS ETGs and their mean value of their dust-to-stellar-mass ratio ($\log(M_d/M_*) = -2.95$, Figure 8) is also larger. Many of their sources have bluer UV–optical colors than the HRS (with a significant fraction lying below NUV $- r < 4$: their Figure 15), suggesting that the larger amount of dust in the H-ATLAS galaxies is associated with increased star formation (Rowlands et al. 2012). The simplest explanation of the differences is that the H-ATLAS study is picking up the rare, very dusty ETGs, which the HRS misses, partly because it is not large enough, and possibly also because it is dominated by the ETGs in the Virgo Cluster. A possible local example of these rare dusty ETGs is the local elliptical Cen A (Parkin et al. 2011). Since the depth of the SDSS images used for the morphological classification in the H-ATLAS study made it impossible to distinguish between ellipticals and S0s, it is also possible that some of the ETGs detected in H-ATLAS are S0s or early-type spirals rather than ellipticals.

Rowlands et al. (2012) were also able to estimate the dust masses of the ETG population *as a whole* using a stacking analysis. They estimated a mean dust mass of $10^{6.3}\,M_\odot$, with a mean dust temperature of 25 K and a mean dust-to-stellar-mass ratio of $\log(M_d/M_*) = -4.87$. This is in reasonable agreement with the average parameters of the early-type sample from this work and in particular, with the S0+S0a sample and our most dusty ellipticals (Figure 8).

4.1. Dust and Stellar Mass along the Hubble Sequence

The average dust mass for the S0+S0a and elliptical galaxies detected by *Herschel* is $10^{6.3}\,M_\odot$ and $10^{5.5}\,M_\odot$ (Figure 7, Table 5) with average dust temperatures of 23.5 and 25.7 K, respectively. The dust masses for the two morphological groups are significantly different (Mann–Whitney $U = 117$ with $n_1 = 6$,

[22] Using the Mann–Whitney U statistic, appropriate when comparing two groups where the underlying distribution of the data is not necessarily normal. The statistic assumes that the observations are independent and are continuous (i.e., able to be ranked) and is more robust than the Student's t-test.

Table 5
Mean Parameters for the Sample

Type	N	T_d (K)	$\log M_d$ ($M_\odot$)	$\log M_*$ ($M_\odot$)	$\log M_d/M_*$	$\log L_X$ (erg s^{-1})	$\log M_{H_2}$ ($M_\odot$)	$\log M_{H\,I}$ ($M_\odot$)
Detected sample:								
Total	31	23.9 ± 0.8	6.12 ± 0.12	10.49 ± 0.07	-4.33 ± 0.13	40.02 ± 1.17 (15)	...	8.40 ± 0.17 (15)
E (+E/S0+pec)	7	25.7 ± 2.5	5.54 ± 0.28	10.89 ± 0.19	-5.26 ± 0.24	40.96 ± 3.11 (5)	<7.21 (0)	8.26 ± 0.14 (5)
S0 (+pec)	24	23.5 ± 0.8	6.26 ± 0.13	10.40 ± 0.06	-4.13 ± 0.12	39.34 ± 1.90 (10)	7.84 ± 0.25 (16)	8.47 ± 0.19 (10)
Entire sample:								
Total	62	...	5.59 ± 0.09	10.09 ± 0.12	-5.12 ± 0.14	39.89 ± 0.18	7.13 ± 0.67 (57)	7.57 ± 0.11 (48)
E (+E/S0+pec)	22	...	5.21 ± 0.09	10.66 ± 0.13	-5.83 ± 0.11	40.13 ± 0.24	7.02 ± 1.29 (21)	7.72 ± 0.17 (15)
S0 (+pec)	39	...	5.87 ± 0.13	10.38 ± 0.04	-4.42 ± 0.10	39.25 ± 0.24	7.25 ± 0.75 (36)	7.58 ± 0.13 (33)

Notes. Top: the mean parameters for the detected sample of early types. Bottom: the mean parameters estimated using survival analysis, including the upper limits. The error quoted is the standard error of the mean. The columns are as follows. Column 1: morphological type. Column 2: the number of sources. Column 3: the average dust temperature. Column 4: the average dust mass (dust masses are estimated using a single temperature modified blackbody with $\beta = 2$ and $\kappa_{350} = 0.19\,\mathrm{m^2\,kg^{-1}}$). Column 5: the average stellar masses using the optical colors (L. Cortese et al., in preparation). Column 6: the average dust-to-stellar-mass ratio. Column 7: average X-ray luminosity—the numbers in brackets give the number of sources with X-ray *and* 250 μm detections. Column 8: the average molecular gas masses estimated from the CO data. Column 9: the average atomic gas masses estimated from H I data.

Table 6
Results of the Two-sample Tests

Sample	Parameter	P(GGW)	P(LR)	P(PPGW)
S0 × E	M_d	0.0005	0.0006	0.004
	M_d/M_*	0.000	0.000	0.000
	$M(H_2)$	0.007	0.009	0.003
Virgo × not Virgo	M_d	0.14	0.09	0.14
	M_*	0.189	0.151	0.165
	M_d/M_*	0.055	0.082	0.078
	M(H I)	0.008	0.011	0.005

Notes. The S0+S0a versus elliptical (top) and Virgo versus non-Virgo galaxy samples tested for the probability they are drawn from the same population. The tests include GGW: Gehan's Generalized Wilcoxon test; LR: log-rank test; PPGW: Peto and Peto Generalized Wilcoxon test. These are determined using the IRAF STSDAS task TWOSAMPT.

$n_2 = 24$ at $P > 99.7\%$ for two-sided test; see footnote 22). This does not take into account the large number of upper limits so we have used the Astronomical Survival Analysis programs (Feigelson & Nelson 1985), implemented through the IRAF STSDAS STATISTICS package, to compare the two samples. Using three different tests we find that the probabilities that the elliptical and S0+S0a dust masses are drawn from the same population are 0.0005, 0.0006, and 0.004, and for M_d/M_*, the probabilities are zero (Table 6); these parameters for S0+S0a and ellipticals in our sample almost certainly arise from different distributions. We have used the Kaplan–Meier estimator[23] to estimate the mean[24] for the two samples, making the necessary approximation that the lowest upper limit is actually a detection. With this approximation, we find that the mean dust mass for the S0s is $10^{5.87}\,M_\odot$ and the mean dust mass for the ellipticals is $10^{5.21}\,M_\odot$ (Table 5).

[23] It is likely that the censoring in this data set is not random: the censored data are a multiple of the noise in the data and we have observed to a flux limit in K with shorter integration times for the S0+S0a sample compared to the ellipticals. The censored data may have some randomization introduced by the SED-fitting technique since the SED can have different distributions but still give the same M_d. We note that the censored data could be biased.

[24] The median of the distribution function returned by Kaplan–Meier estimator is well defined if the censored data are restricted to less than half of the sample. Given the small sample size of the ellipticals which is dominated by upper limits (70% of the data) we use the mean in this work.

C12 has recently shown that the dust-to-stellar-mass ratio decreases when moving from late- to early-type galaxies, but used a conservative approach by treating non-detections as upper limits. Here we incorporate the information in the upper limits on the non-detected sources and quantify the change as we move along the Hubble sequence. We estimate that the mean value[24] of the dust-to-stellar-mass for the ellipticals is $\log(M_d/M_*) = -5.83 \pm 0.1$ and for the S0s is -4.42 ± 0.1 (Table 5).

Following C12 (his Figure 5), we plot the dust-to-stellar-mass ratio against morphological type in Figure 9. We split the late-type sample into the subgroups: Sa+Sab, Sb+Sbc, Sc+Scd, and Sd+Sdm. The figure also shows the strong drop in mean dust-to-stellar-mass ratio from early-type spirals to S0s (and the further decline as we move to ellipticals). Figure 9 suggests that the variation in this ratio is larger for early types than late types. This is particularly true for early-type spirals and S0+S0a galaxies with M_d/M_* ranging by a factor of approximately 50. Although ellipticals probably have a similarly wide range in dust-to-stellar-mass, the high number of non-detections make it difficult to be sure of this.

4.2. The Origin of Dust in ETGs

One of the big questions about dust in ETGs is its origin. There are three main possible sources: (1) the dust is formed in the old stellar population in the atmospheres of AGB stars, (2) the dust is acquired externally as the result of a galaxy merger or a tidal interaction, and (3) the dust has the same rather uncertain sources as in late-type galaxies (e.g., Morgan & Edmunds 2003). In (3), the dust might be continuously created by grain growth in the ISM or current star formation via dust production in supernovae (e.g., Barlow et al. 2010; Matsuura et al. 2011; Gomez et al. 2012), or it might be left over from a more vigorous star-forming epoch. The strongest prediction is made by the first hypothesis, since this makes the clear prediction that there should be a strong correlation between dust mass and stellar mass.

To test point (1) we compare the FIR emission from the dust with the starlight and the emission from the hot ISM. If the source of the hot gas is mass loss from stars, one would expect the X-ray luminosity (L_X) to correlate with the optical luminosity (L_B), which is true for our sample (Appendix B, Equation (B1)). Similarly, if the source of the dust is stellar mass loss, we would expect to see a correlation between dust

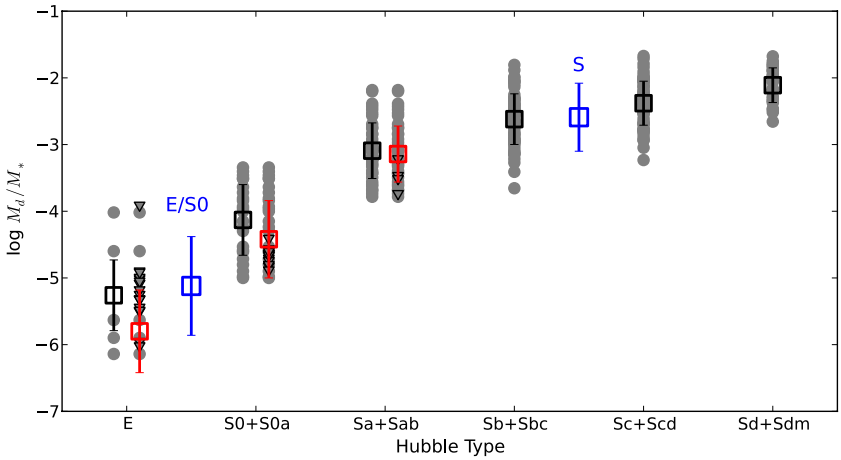

Figure 9. Dust-to-stellar-mass ratio vs. morphological type for the detected and undetected sources. Gray circles show the M_d/M_* estimated for detected sources, with upper limits highlighted with gray triangles. The mean and standard deviation of M_d/M_* for the *detected* samples are highlighted with black boxes and error bars. Offset from the detected sources, we also show the entire HRS sample in each Hubble type including both detected sources and upper limits. The mean and standard deviation for the samples *including* the upper limits are shown with the red squares and error bars (see Table 5). We also compare the mean and standard deviation of the complete early-type galaxies (S0+S0a and E) and the complete sample of spiral galaxies (C12) in blue. The stellar masses are from L. Cortese et al. (in preparation).

mass and optical luminosity; alternatively, a lack of correlation may indicate that mergers are important for delivering dust.

The FIR luminosity, $L_{\rm FIR}$ (Table 4) was determined by integrating over the SED (Figures 5 and 6). (This is an underestimate of the total IR luminosity as the 70 μm fluxes are treated as upper limits in our SED fitting; we estimate that including a warm temperature component to fit the MIR–70 μm emission would contribute (on average) 3% to the FIR luminosity, though for some sources this can be up to 17%—see also Muñoz-Mateos et al. 2009.) The mean ratio of FIR to optical luminosity $\log(L_{\rm FIR}/L_B)$ for S0s is -1.1 ± 0.1 and -2.2 ± 0.1 for ellipticals; therefore ellipticals have less FIR luminosity per unit blue luminosity than S0s (also seen in an *IRAS* sample of isolated galaxies; Lisenfeld et al. 2007). In Figure 10, we compare the $L_{\rm FIR}$ with the optical luminosity which does indeed increase as L_B increases, but the large scatter suggests that dust may have been acquired from tidal interactions or mergers as well as stellar mass loss. There is no evidence of a correlation between $L_{\rm FIR}$ and L_B (Figure 10, Appendix B). We also find no correlation with $L_{\rm FIR}$ and the X-ray luminosity L_X.

Since $L_{\rm FIR}$ depends strongly on the temperature of the dust, it is instructive to compare the dust mass, M_d, with the optical and X-ray luminosities (Figure 10; Equations (B4) and (B5)). We find that the dust mass increases weakly with L_B, but there is no statistical correlation between the two. The same is true for M_d and L_X. We compare the predicted relationships for a model in which dust is replenished by stellar mass loss from evolved stars and destroyed by dust sputtering (Goudfrooij & de Jong 1995; Figure 10). The mass of gas lost in these winds is estimated by $\dot{M}_{\rm gas} = 1.5 \times 10^{-11}(L_B/L_\odot)\, M_\odot\ {\rm yr}^{-1}$ (Faber & Gallagher 1976), which ranges from 0.005 to 0.75 $M_\odot\ {\rm yr}^{-1}$ for the HRS ellipticals.[25] The estimates of the final dust masses depend critically on the assumption of the lifetime of the dust: dust destruction in a hot plasma probably occurs on timescales of $\tau_d \sim 10^6$–10^7 yr (Draine & Salpeter 1979). Goudfrooij & de Jong note that $\tau_d \sim 10^{7.5}$ yr is the maximum plausible destruction timescale since this corresponds to electron densities in the hot X-ray plasma $n_{\rm H} < 10^{-3}\ {\rm cm}^{-3}$. In the figure we plot the predicted relationships for values of $\log_{10}(\tau_d)$ from 6.5 to 7.5. The ETG sample detected by *Herschel* have dust masses well above the theoretical curves, suggesting an alternative source of dust is needed for most of the sources. Longer grain lifetimes for some of the galaxies may also occur if a significant component of cool gas exists (see Section 4.3); in this case dust may reside in conditions similar to the Milky Way, with destruction timescales of the order of $\log_{10}(\tau_d) = 8.5$. Three elliptical galaxies have dust masses consistent with the boundary marked by the maximum destruction timescale $\log_{10}(\tau_d) = 7.5$. Note that the figure shows that dust originating from AGB-stellar mass loss (Clemens et al. 2010) could be consistent with the upper limits estimated for 50% of the ETGs.

We conclude then that there is no strong statistical evidence of a correlation in FIR luminosity or dust mass with blue- or X-ray luminosity. The dust masses of the ETGs detected by *Herschel* are also larger than the estimates from a model in which dust is produced from stellar mass loss from evolved stars, even with the most generous assumption about how long the dust grains will survive in the ISM. Furthermore, if the dust in ETGs is in equilibrium, with dust formation in old AGB stars balanced by dust destruction via sputtering, we would also expect a small range in M_d/M_*. Figures 8 and 9 show that the variation in this ratio is much larger for early types than late types; this is particularly true for S0 galaxies with M_d/M_* ranging by a factor of ∼50. Finally, another argument against hypothesis (1) and the supernova origin of dust in hypothesis (3) is that if stellar mass loss was responsible for the dust, the dust would be distributed in a similar way to the stars. However, for five of the six ellipticals in which *Herschel* has detected dust (excluding M87), there is evidence from the appearance of the dust in absorption against the optical or near-IR continuum emission that the dust is distributed in a different way from the stars (see Appendix A).

The evidence therefore points toward a merger origin of dust in this sample; this is supported by evidence from other recent studies that the cool ISM in ETGs may have been acquired as the result of gravitational interactions. For example, Davis et al. (2011) have used the misalignment between the kinematics of the stars and the gas in ETGs to conclude that at least one-third of ETGs have acquired much of their ISM by this means.

[25] We assume that the gas-to-dust ratio in the stellar winds of evolved stars is ∼150.

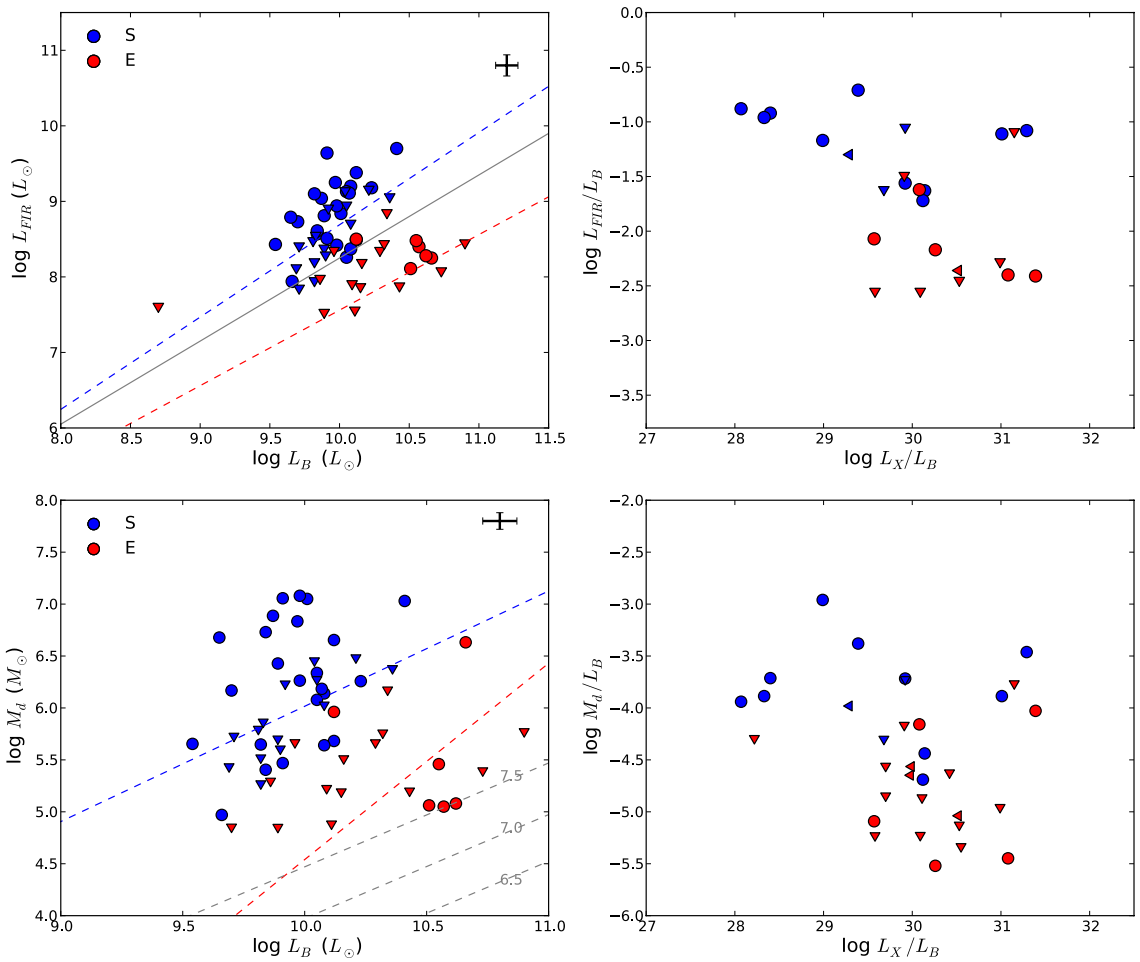

Figure 10. Top panel: the FIR luminosity from the cold dust component $L_{\rm FIR}$(cold) vs. the *B*-band luminosity (left). Blue points are S0+S0a galaxies and red points are the ellipticals. Upper limits are plotted as downward-pointing triangles. The gray solid line shows the expected relationship (arbitrarily normalized) for $L_{\rm FIR} \propto L_B^{1.1}$ if the FIR emission is produced by dust from stellar atmospheres. The best-fit line to the S0+S0a sample including the upper limits is shown by the dashed blue line ($m = 1.22, c = -3.53, \sigma_r = 0.39$) as estimated from the Buckley James method. The correlation parameters for ellipticals are shown by the dashed red line ($m = 1.00, c = -2.44, \sigma_r = 0.3$). Right: the FIR emission vs. X-ray luminosity (L_X) normalized by the blue luminosity (L_B). Bottom panel: the dust mass M_d vs. the *B*-band luminosity (left) and vs. X-ray luminosity (right). The logM_d vs. logL_B relationship is described with $m = 1.11, c = -5.08$, and $\sigma_r = 0.58$ for the S0+S0a (blue dashed) and $m = 1.89, c = -14.40$, and $\sigma_r = 0.97$ for the ellipticals (red dashed). The dashed gray lines represent the loci where dust is replenished by stellar mass loss and destroyed by dust sputtering in the hot gas (the labels represent the log of the dust destruction timescale assumed). This model assumes a gas-to-dust ratio of 150. The errors on the dust mass are similar to the symbol size for most galaxies, and a representative error bar is shown.

4.3. A Cool Interstellar Medium in Early-type Galaxies?

In the last decade, it has become clear that a significant fraction of ETGs do contain a cool ISM similar to that of spirals. Morganti et al. (2006) detected H I in 70% of their sample of nearby ETGs (see also Oosterloo et al. 2010; Serra et al. 2009; di Serego Alighieri et al. 2007) and detections of molecular gas have been made in many (Sage et al. 2007; Lucero & Young 2007; Combes et al. 2007). A number of studies indicate ongoing star formation in a significant fraction of ETGs (Kaneda et al. 2005, 2008; Bressan et al. 2006; Panuzzo et al. 2007, 2011; Temi et al. 2007a, 2007b) and the detection of dust in 50% of our sample strongly supports the conclusion that a significant fraction of ETGs contain a cool ISM.

We can compare the ISM in the ETGs with that in late types in two other ways. First, using the measurements of the dust, atomic, and molecular gas that exist for eight galaxies from our sample (Table 4), we estimate that the mean gas-to-dust ratio is $10^{2.08\pm0.08}$, similar to the typical value for late-type galaxies: ∼100–200.

Second, in late-type galaxies there is a tight correlation between FIR and radio emission (Wrobel & Heeschen 1988; Helou et al. 1985; Devereux & Eales 1989). This is usually explained as the result of a correlation between the FIR emission and the SFR, with FIR emission originating either from dust heated by young stars (e.g., Vlahakis et al. 2007 and references therein; G. P. Ford et al. in preparation) or due to dust itself tracing the gas mass, which in turn fuels star formation (Rowan-Robinson et al. 2010; Bendo et al. 2012). The radio emission is then also correlated with the SFR as it originates from relativistic electrons produced by supernova remnants after the young stars die. Whether or not this correlation is truly caused by the SFR, we can at least see whether the ETGs in our sample have a similar ratio of FIR–radio as spiral galaxies. Sixteen ETGs are detected at 1.4 GHz (see Figures 1 and 2) by the Faint Images of the Radio Sky at Twenty centimeters (FIRST) radio survey (Becker et al. 1995). For these sources we have estimated the value of the parameter, q, introduced by Helou et al. (1985), defined as

$$q = \log\left(\frac{L_{\rm FIR}}{3.75 \times 10^{12}\,{\rm W\,m^{-2}}}\right) - \log\left(\frac{L_{1.4\,{\rm GHz}}}{{\rm W\,m^{-2}}}\right), \qquad (2)$$

where $L_{\rm FIR}$ and $L_{1.4\,{\rm GHz}}$ are the FIR and radio luminosities, respectively. Yun et al. (2001) found a median value for nearby

galaxies of $q = 2.64 \pm 0.02$, with most star-forming galaxies having values of q between 2 and 3. Wrobel & Heeschen (1988), and more recently Combes et al. (2007) and Lucero & Young (2007), have found similar values of q for ETGs in which star formation is occurring.

Two of our galaxies (NGC 4636, NGC 4374) have $q < 1.8$, which suggests they host radio-loud AGNs. Of 16 sources with FIRST detections in our HRS sample out, 13 have $2.15 < q < 3.32$, similar to star-forming late types. Nine of these sources also have CO detections (Table 4) and therefore 70% of the galaxies which the q values suggestive of star formation also have a reservoir of molecular gas. These galaxies lie below the "quiescent" UV–optical boundary defined as NUV $- r < 5.4$ (Section 3.2) and a literature search reveals evidence of residual star formation in seven out of the nine galaxies, with signatures including mid-IR emission (Panuzzo et al. 2007; Shapiro et al. 2010), line diagnostics (Sil'chenko et al. 2010; Crocker et al. 2011), and UV emission (Cortese & Hughes 2009).

Converting the q ratio into SFRs for ETGs is extremely complex due to the difficulty in disentangling the AGN component, other processes that may be heating the dust, and the thermal contribution to the radio emission. If the $q \sim 2$ ratios for those galaxies with molecular gas are an indication of star formation, then there are not only cool gas and dust in these galaxies but also stars forming at a measurable rate for at least 15% of the sample. We defer a full analysis of SFRs for future work, though we note that a literature search reveals SFRs ranging from 0.03 to 0.40 $M_\odot\,\mathrm{yr}^{-1}$ in 23% of the HRS ETG sample (see references listed above).

In summary, although the mass of the ISM in ETGs is less than the mass of the ISM in late types, observations of the radio continuum, CO, and H I are consistent with the ISM in ETGs being quite similar to that found in late types. The only difference is that, on average, the dust in ETGs has a temperature that is a few degrees higher, possibly due to the dust grains in early types being exposed to a more intense interstellar radiation field or from the more centrally distributed dust emission in ETGs (e.g., Sauvage & Thuan 1992; Bendo et al. 2011).

5. DISCUSSION

5.1. Evidence for Dust-depleted Disks in S0s

The large fall in the dust-to-stellar-mass ratio between early-type spirals and S0+S0a galaxies (Figures 8 and 9) suggests that S0s contain a smaller mass of ISM per mass of stars than early-type spirals (i.e., those with Hubble type ranging from Sa to Sbc). However, the bulge-to-total mass ratio is known to be larger for S0s than early-type spirals: Is the fall in the dust-to-stellar-mass ratio we observe here simply a reflection of the more massive bulges of S0s? We can test this idea by making the assumptions that (1) bulges do not contain dust and (2) the dust-to-stellar-mass ratio is the same for all disks. With these assumptions, to explain the factor of 10 decrease in the dust-to-stellar-mass ratio of S0s relative to early-type spirals, the bulge-to-total stellar-mass ratio must change by a very large factor. If the bulge-to-total stellar-mass ratio is 0.1 for early-type spirals, it must be 0.91 for S0s. For larger values of the bulge-to-disk stellar-mass ratio for the early-type spirals (Sa–Sc), even larger ones are required for the S0s. Weinzirl et al. (2009) have found that the proportion of the total mass of a galaxy that is in the bulge increases from ∼0.1 for Sbc galaxies to ∼0.2 for S0+S0a galaxies (their Figure 14). In larger samples, Graham & Worley (2008) and Laurikainen et al. (2010) find values for this

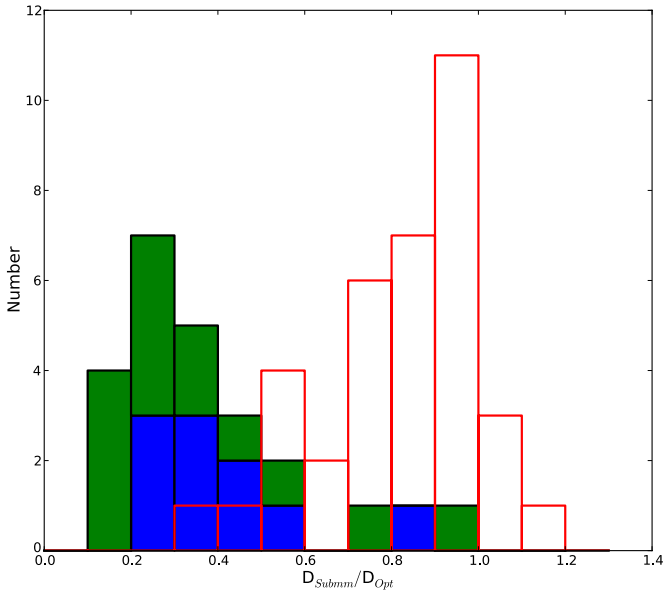

Figure 11. Ratio of the submm and optical sizes for the HRS sample. The red histogram shows the distribution of $D_{\mathrm{submm}}/D_{\mathrm{opt}}$ for the early-type spiral galaxies (Sa-Sbc) with the same color cut as the S0 and ellipticals, i.e., $K < 8.7$ (the original sample of early types is presented in Cortese et al. 2010b and C12). The green shaded histogram shows the distribution for the S0s in this paper, with the blue shaded histogram showing the S0s that are not in one of the Virgo clouds or the outskirts of Virgo (Boselli et al. 2010b).

ratio of approximately 0.1–0.2 for Sab–Sbc galaxies and 0.3–0.5 for S0 galaxies (their Figure 4), a somewhat larger change but still too low to explain the different dust-to-stellar-mass ratios.

Another way to investigate this is to compare the ratio of the submm diameter to the optical diameter (e.g., Cortese et al. 2010b), where the optical diameter is likely to be a good measure of the size of the disk. We measured this ratio for two samples: (1) all of the S0 galaxies and (2) all early-type spiral galaxies in the HRS with $K < 8.7$ (the limit used for ETGs). For the optical size of the galaxy we used θ_{major}, the diameter along the major axis measured to the standard B 25th mag arcsec^{-2} isophote ($D(25)$). For the submm size, we used the same definition, finding the ellipse that provided the best fit on the 250 μm image to an isophotal brightness of 6.7×10^{-5} Jy arcsec^{-2}. Figure 11 shows the distributions of $D_{\mathrm{submm}}/D_{\mathrm{opt}}$ for the S0+S0a galaxies and the early-type spirals with the same K-band magnitude selection; these populations are significantly different ($P < 0.001$ level[26]). We do not apply a correction for beam smearing, which increases the angular sizes of the objects, an effect which is biggest for the objects with smallest angular size. If a correction was made for this bias, the difference between S0+S0a and early-type spiral populations seen in Figure 11 would increase. We have also compared the submm–optical sizes for the S0 galaxies outside of Virgo in Figure 11. The values for these are still clearly different from the early-type spirals, strongly suggesting that the dust-depleted disks of S0s are not caused by a current cluster-environmental effect.

Both approaches imply that the dust-to-stellar-mass ratio is lower for the disks of S0 galaxies than the disks of early-type spirals, suggesting that the disk of an S0 contains a smaller mass of ISM than the disk of an early-type spiral with the same stellar mass. This is not an entirely surprising result, since for the last

[26] Using the Kolmogorov–Smirnov two-sample test.

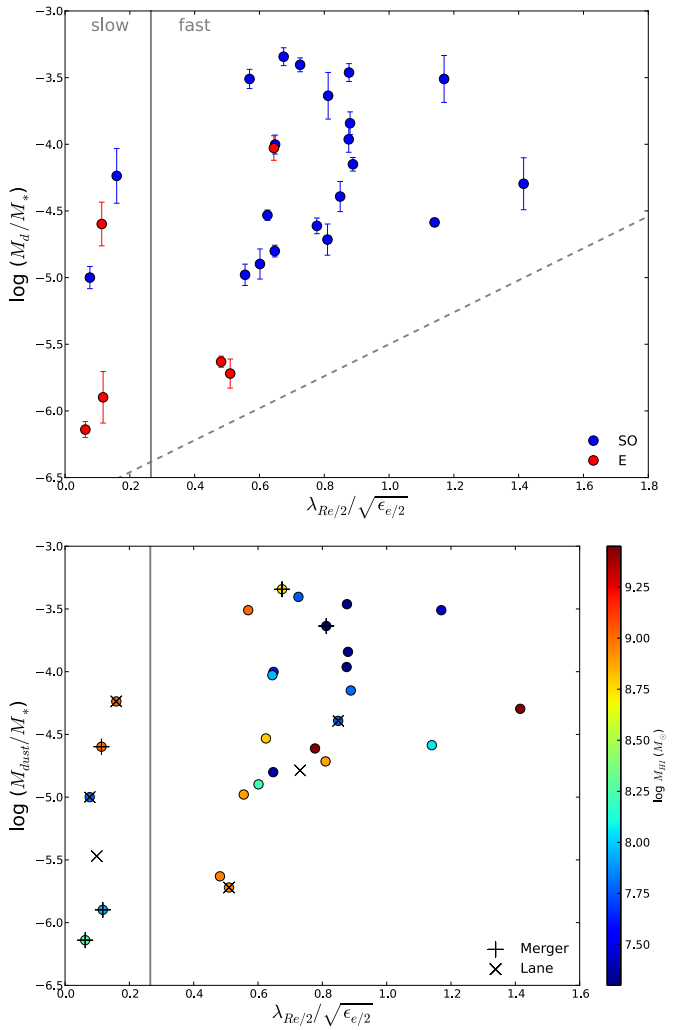

Figure 12. Top: the dust-to-stellar-mass ratio vs. the kinematical parameter $\lambda_{Re/2}/\sqrt{\epsilon_{e/2}}$, where $\epsilon_{e/2}$ is the ellipticity measured within an aperture defined at 0.5 R_e and R_e is the effective radius of the galaxy. λ_R is a proxy for the angular momentum per unit stellar mass and the $\sqrt{\epsilon_{e/2}}$ term accounts for the shape of a galaxy since a more flattened galaxy would be expected to have a stronger anisotropy. Blue points are S0+S0a galaxies and red points are ellipticals. The gray solid line marks the region defined as the boundary between fast and slow rotators (Emsellem et al. 2011), i.e., between galaxies with disk-like rotation and bulge-like kinematics. Bottom: as above but color-coded with respect to the H I mass. Galaxies which are known to be mergers or have obvious dust lanes in the optical are indicated with "+" (mergers) and "×" (dust lanes). Galaxies without filled circles are the *Herschel*-detected galaxies that have no corresponding H I observations. Many of the galaxies at the lower end of the H I mass scale are upper limits (Table 4). The gray dashed line roughly marks the detection limit of the survey and note that NGC 4486 (HRS183) is not shown in these plots.

40 years the working definition of an S0 galaxy is that it is a galaxy with a disk but no sign of spiral arms or, if it is an edge-on galaxy, of a dust lane (Sandage 1961). Nevertheless, even if the qualitative result is not surprising, *Herschel* has allowed us to determine how little ISM the disks of S0 galaxies do contain.

5.2. Ellipticals and S0s or Slow Rotators and Fast Rotators?

So far in this paper, we have classified ETGs based on their optical morphology into ellipticals and S0s. Based on the ATLAS^{3D} study of the stellar kinematics of 260 ETGs, Cappellari et al. (2011) have argued that a physically more meaningful way is to divide ETGs into slow rotators and fast rotators. Emsellem et al. (2011) found that 66% of the galaxies in ATLAS^{3D}, which are traditionally morphologically classified as ellipticals, have disk-like kinematics and are therefore fast rotators. Given the similarity in the kinematics, the suggestion is then that early-type fast rotators are part of the same evolutionary sequence as the late types, but are at different stages of their evolution. Slow rotators are defined as galaxies with bulge-like properties, likely to be the end-point of systems that have undergone complex merger histories; these are massive, lie on the red sequence, and contain very little cool interstellar material.

Eleven (18%) of the ETGs in our sample are slow rotators, including nine ellipticals (39% of the ellipticals) and two S0s (5%). In Figure 12(a), we plot dust-to-stellar-mass ratio versus the quantity $\lambda_{R_{e/2}}/\sqrt{\epsilon_{e/2}}$, where ϵ is the ellipticity of the galaxy and R_e is the effective radius. This parameter is suggested by the ATLAS^{3D} team as appropriate to separate out the slow and fast rotators since it is a good measure of the projected stellar angular momentum per unit mass (Emsellem et al. 2007). There is no sign of a correlation between the two parameters for galaxies in our sample. Indeed, with *Herschel* we have detected dust emission from 50% of the slow rotators, including four ellipticals, which is not very different from the detection fraction for all the ETGs (Table 3).

The fact that there is a clearer distinction in the dust properties of the ETGs when they are put in morphological classes (Figures 8 and 9) than when they are put into kinematic classes does not mean that the kinematic division is not physically meaningful. It is possible that the morphological classification is more connected to the mass of ISM in a galaxy than the kinematic classification, although the kinematic definition may be telling us more about the evolutionary state of the galaxy. As *Herschel* detects a number of slow rotators and the lack of correlation seen in Figure 12(a), this may be additional evidence that the cool ISM in ETGs is acquired by random gravitational encounters. Again, the amount of dust may not be connected with the evolutionary state of the galaxy. In Figure 12(b), we show the same diagram but this time labeling the galaxies by their H I mass. There is a tendency for galaxies with larger atomic gas masses to have higher dust-to-stellar-mass ratios. Since the 21 cm morphologies have often been adduced as evidence for an external origin of the ISM (e.g., Serra et al. 2009), this figure may be additional evidence that the mass of the ISM is rather unconnected to the evolutionary history of the stellar populations in the galaxies.

Finally, we note that connections between the dust properties and stellar kinematics of the ETGs may become evident in a larger sample. The HRS sample of ETGs is a statistically complete quasi-volume-limited sample, but the volume contains the rich environment of the Virgo Cluster and is therefore not a representative sample of the local universe. The HRS ETGs also cover a limited range of stellar mass (Section 3, Figure 3). An important future project would be to observe the dust in a sample of ETGs containing more galaxies in low-density environments and with a wider range of stellar mass.

5.3. Galaxy Evolution

We can use the results from the *Herschel* observations to make an inference about the evolution of early types. On the assumption that the dust we observe is delivered to the galaxies externally, we can make a rough estimate of the effect such an interaction would have on the stellar mass of the ETG. We use the mean values of M_d/M_* shown in Figure 9 (Table 5) for the different morphological classes ($10^{-5.9}$ for ellipticals, $10^{-4.4}$ for S0s, and $\sim 10^{-3.0}$ for spirals). On the assumption that all the dust

we detect in an ETG is the result of a past merger with a spiral, the ratio of the mass of the spiral to the original ETG must be ∼0.05 for an elliptical and ∼0.1 for an S0. These estimates suggest that such interactions are only minor mergers and do not represent significant galaxy-building events. The estimates are also upper limits because the dust may have been acquired by a tidal interaction without the galaxies necessarily merging, and some of the dust may also have been produced inside the galaxy.

6. CONCLUSIONS

We present the FIR and submm observations with *Herschel* of 62 ETGs, including 23 ellipticals and 39 S0+S0a galaxies. We find the following results.

1. We detect 24% of the ellipticals and 62% of the S0s. The optical and X-ray luminosities of the detected sources show we are detecting the most massive ellipticals, though the S0 sample is representative of the general population. Of the 10 "pure" ellipticals in our sample only 1 is detected by *Herschel* (M86), while 6 of the 11 "impure" ellipticals are detected. The detection rate for the ETGs outside Virgo appears to be higher than for those inside the cluster, but this is not statistically significant.
2. The mean dust masses for the detected galaxies are $\log M_d = 6.3 \pm 0.1$ and $5.5 \pm 0.3\,M_\odot$ for the S0+S0a and E population, with average dust-to-stellar-mass ratios of $\log(M_d/M_*) = -4.1 \pm 0.1$ and -5.3 ± 0.2. Including the upper limits, the average dust masses for the detected *and* undetected S0+S0a and elliptical sources are $\log M_d(M_\odot) = 5.9 \pm 0.1$ and 5.2 ± 0.1, with dust-to-stellar-mass ratios of $\log(M_d/M_*) = -4.4 \pm 0.1$ and -5.8 ± 0.1.
3. The mean dust temperature for the ETGs *detected* by *Herschel* is ∼24 K, warmer than the dust in late-type galaxies. The *entire* early-type sample, including non-detections, has a dust mass of $\log M_d = 5.6 \pm 0.1$ and $\log(M_d/M_*) = -5.1 \pm 0.1$. In comparison, the average dust-to-stellar-mass ratio for spiral galaxies in the HRS is -2.59 ± 0.03. The dispersion in the dust-to-stellar-mass ratio is much greater for ETGs than spirals.
4. The NUV − r colors show that virtually all the ETGs lie close to the red sequence, but there is evidence from UV and optical colors, radio continuum observations, and literature searches that a ∼20% of the sample have had a recent star-forming epoch or have significant residual star formation. However, the NUV colors have not been corrected for extinction or contamination from the old stellar population. Our ETGs are redder in NUV − r with lower dust-to-stellar-mass ratios than the ETGs detected in the H-ATLAS survey.
5. We show that the detection of cold dust, the ratio of far-infrared to radio emission, and the gas-to-dust ratios all indicate that many ETGs contain a cool ISM in which stars are forming, similar to that seen in spiral galaxies.
6. We find no evidence for a correlation between the FIR luminosity or dust mass of ETGs with the optical luminosity, suggesting that the main source of the dust in the galaxies detected by *Herschel* is not mass loss from evolved stars. This, together with the large spread in the dust-to-stellar-mass ratio of ETGs, suggests a significant fraction of the dust in these galaxies is acquired externally via mergers or tidal interactions.
7. We use the results from the ATLAS^{3D} survey to divide our sample into fast and slow rotators. We show that the difference in dust properties between S0s and ellipticals is more obvious than the difference between slow and fast rotators. We suggest that this may be additional evidence that the dust in ETGs has been acquired by gravitational encounters and may not tell us much about the evolutionary state of the galaxy.
8. The low dust-to-stellar-mass ratios of S0s compared with early-type spirals cannot be explained by the larger bulge-to-disk ratios of S0s. The relative sizes of the dust sources in S0s are also smaller than seen in early-type spirals. These suggest that the disks in S0s contain much less dust (and presumably gas) than spiral disks with a similar size. This effect is probably not being caused by current environmental processes adding to the weight of evidence that early-type spirals are not being transformed into S0s in significant numbers at the current epoch.
9. If the cool ISM in ETGs is acquired as the result of a tidal interaction or merger, an upper limit on the increase in the stellar mass of the ETG due to the interaction is 1% for the ellipticals and 10% for the S0s, suggesting that the interactions are not significant galaxy-building events.

Our sample of ETGs has lower dust-to-stellar-mass ratios and dust masses compared to previously published *Herschel* samples. The results from our sample are important for interpreting chemical evolution models which model the production and destruction of dust in ellipticals as well as providing a low-redshift benchmark for understanding the evolution of dust and gas in high-redshift surveys (e.g., Rowlands et al. 2012; Dunne et al. 2011). Finally, we note that to obtain a better understanding of some of these issues it will be important to follow up our statistical study with detailed observational studies of individual ETGs, for example with ALMA (Atacama Large Millimeter/submillimeter Array).

We thank everyone involved with the *Herschel* Observatory. PACS has been developed by a consortium of institutes led by MPE (Germany) and including UVIE (Austria); KU Leuven, CSL, IMEC (Belgium); CEA, LAM (France); MPIA (Germany); INAF- IFSI/OAA/OAP/OAT, LENS, SISSA (Italy); and IAC (Spain). This development has been supported by the funding agencies BMVIT (Austria), ESA-PRODEX (Belgium), CEA/CNES (France), DLR (Germany), ASI/INAF (Italy), and CICYT/MCYT (Spain). SPIRE has been developed by a consortium of institutes led by Cardiff University (UK) and including the University of Lethbridge (Canada); NAOC (China); CEA, OAMP (France); IFSI, University of Padua (Italy); IAC (Spain); Stockholm Observatory (Sweden); Imperial College London, RAL, UCL-MSSL, UKATC, University of Sussex (UK); and Caltech/JPL, IPAC, and the University of Colorado (USA). This development has been supported by national funding agencies: CSA (Canada); NAOC (China); CEA, CNES, CNRS (France); ASI (Italy); MCINN (Spain); Stockholm Observatory (Sweden); STFC and UKSA (UK); and NASA (USA). HIPE is a joint development by the *Herschel* Science Ground Segment Consortium, consisting of ESA, the NASA *Herschel* Science Center, and the HIFI, PACS, and SPIRE consortia. This research made use of the NASA/IPAC Extragalactic Database (NED: http://ned.ipac.caltech.edu/) which is operated by the Jet Propulsion Laboratory, California Institute of Technology, under contract with the National Aeronautics and Space Administration. The research leading to these results has received funding from

the European Community's Seventh Framework Programme (/FP7/2007-2013/) under grant agreement No. 229517. This research made use of APLpy, an open-source plotting package for Python hosted at http://aplpy.github.com. We thank Edward Gomez for useful and informative discussions and H.L.G. acknowledges the support of Las Cumbres Observatory.

Facilities: Herschel (PACS, SPIRE), *Spitzer* (MIPS), *IRAS*

APPENDIX A

NOTES ON THE ELLIPTICALS DETECTED BY *HERSCHEL*

HRS3, NGC 3226. A semicircular lane of dust in NGC 3226 is seen as absorption in the optical (Martel et al. 2004) with dusty strands extending north–south. The source is known to be interacting with the nearby spiral NGC 3227 (the bright source to the south of the elliptical—Figure 2), which has clear tidal gas trails (Mundell et al. 2004). The elliptical appears slightly extended in the 250 μm image but more compact than in the optical image (Figure 2). NGC 3226 is part of the Leo Cloud.

HRS138, NGC 4374 (M84). M84 has a radio bright core and radio jets. *Hubble Space Telescope* (*HST*) images show dust lanes across the center of the galaxy (Bower et al. 1997), which are approximately perpendicular to the radio jet. The galaxy was detected at 850 μm with SCUBA by Leeuw et al. (2000). They concluded that most of the 850 μm flux was synchrotron emission, but that the emission at shorter wavelengths detected by *IRAS* was produced by $\sim 10^5\ M_\odot$ of dust at a temperature of 35 K (see also Boselli et al. 2010a). The 250 μm source is unresolved and is coincident with the radio core (Figure 2). NGC 4374 is a member of the Virgo Cluster.

HRS150, NGC 4406 (M86). M86 is a well-known IR-bright giant elliptical. Two dust features were detected with *IRAS* and originally attributed to dust stripped from M86 due to its motion through the cluster. The discovery of atomic gas offset from the center of M86 and decoupled from its stellar disk supports a tidal interaction (Li & van Gorkom 2001), confirmed when Kenney et al. (2008) detected strong Hα features extending from M86 to the nearby spiral NGC 4438. The distribution and velocity of the ionized gas provide clear evidence for tidal interaction between these two giants. *Herschel*/SPIRE observations of M86 and NGC 4438 showed that the dust emission is spatially correlated with the ionized gas between the two galaxies (Gomez et al. 2010; Cortese et al. 2010a) implying that the dust is material stripped from the nearby spiral. In Figure 2, the appearance of the dust emission in M86 is clearly different from the other ellipticals in our sample, with faint filamentary features seen within $D(25)$. NGC 4406 is a member of the Virgo Cluster.

HRS183, NGC 4486 (M87). M87 is the brightest galaxy in the Virgo Cluster and well known for the jet extending from the nucleus seen at radio, optical, and X-ray wavelengths (Junor et al. 1999). The presence of dust was inferred from *HST* $g-z$ color images (Ferrarese et al. 2006) and the strong FIR emission seen with *Spitzer* (Perlman et al. 2007). The latter result might be explained by synchrotron emission from the central radio source. Although the optical images show dust is present, *Herschel* observations of M87 with PACS and SPIRE as part of HeViCS (Baes et al. 2010; Boselli et al. 2010a) found no evidence of a dust component in excess of the synchrotron emission in the FIR and submm. Baes et al. place an upper limit on the dust mass of $10^5\ M_\odot$. In the *Herschel* image, M87 is a bright, extended source.

HRS186, NGC 4494. NGC 4494 is often described as an "ordinary elliptical" (Capaccioli et al. 1992). O'Sullivan & Ponman (2004) found that its X-ray luminosity was two orders of magnitude lower than expected for its optical luminosity and there are signs of a small dust disk in absorption (Tran et al. 2001). X-ray faint galaxies such as NGC 4494 may arise due to losing their hot X-ray gas in outflows. Further evidence of interactions with nearby galaxies or mergers is the low metallicity estimated from the X-ray gas ($<0.1\ Z_\odot$, O'Sullivan & Ponman 2004), and this may indicate dilution of interstellar material via an infall of unenriched (cold) material. The galaxy is slightly extended at 250 μm. NGC 4494 is a member of the Coma I Cloud.

HRS241, NGC 4636. NGC 4636 has dust features and an unusual X-ray morphology (Temi et al. 2007b). The origin of this morphology is thought to be recent outbursts from the central AGN (Jones et al. 2002). Temi et al. (2003) used *ISO* observations to show that the dust mass for NGC 4636 is far in excess of that expected from stellar mass loss and proposed that the dust was accreted in a very recent merger with a dusty, gas-rich galaxy (similar to M86, Gomez et al. 2010). NGC 4636 is part of the Virgo Cluster.

HRS258, NGC 4697. NGC 4697 is an X-ray-faint galaxy given its optical luminosity, which may be a result of severe loss of interstellar gas via stripping or outflows (Sarazin et al. 2001). As in NGC 4494, the metallicity of the gas is low ($<0.07\ Z_\odot$), pointing toward dilution of the interstellar medium with unenriched cold gas. The source is slightly extended at 250 μm. NGC 4697 is in the outer regions of the Virgo Cluster.

APPENDIX B

FIR EMISSION VERSUS OPTICAL AND X-RAY

We investigated whether there is a correlation between L_X and L_B using the statistics in the ASURV package for dealing with censored data. We find evidence for a correlation for the elliptical galaxies ($P = 99.3\%$[27]). The relationship between the two parameters for ellipticals[28] is described by the following relationship with deviation from the regression $\sigma_r = 0.43$:

$$\log L_B = (2.95 \pm 1.03) \log L_X + 10.79. \quad \text{(B1)}$$

This relationship agrees with other IR samples dominated by massive ETGs (see also Brown & Bregman 1998), whereas X-ray studies indicative of the entire population find are described by $L_X \propto L_B^{2.3}$ (O'Sullivan et al. 2001; Temi et al. 2004).

If the dust produced in ETGs is due to stellar mass loss, the dust mass would be roughly proportional to the mass of the stars, and hence to L_B. If the dust is then widely dispersed and heated by the starlight as well as electron collisions in the hot, X-ray emitting gas, the FIR emission will also depend on the density of the gas or on the stellar density, which are both roughly proportional to $L_B^{1/2}$. Therefore, we would expect $L_{\rm FIR} \propto L_B^{1.4-1.6}$. Bregman et al. (1998) indeed found this

[27] Using the Kendall τ test, a statistic used to measure the association between X and Y; this test is appropriate for small samples with upper limits where the underlying distributions of X and Y are not known.

[28] Using the Buckley–James method, a standard linear regression estimator. This test requires that the censoring distribution about the fitted line is random and does not require the residuals to be Gaussian as other regression methods do.

relationship was true for *IRAS*-detected ETGs, though Temi et al. 2004 found no correlation for their *ISO*-detected sources. In the *Herschel* sample, we see that the FIR luminosity of S0+S0a galaxies does appear to increase with the optical luminosity, although this is not a statistical correlation, with Spearman rank[29] coefficient $r_S = 0.36$ and probability that a correlation is present of $P = 97\%$. The S0+S0a data can be fit by the following equation[28] with $\sigma_r = 0.39$:

$$\log L_{\rm FIR}({\rm S0}) = (1.22 \pm 0.42)\log(L_B) - 3.53. \quad \text{(B2)}$$

The FIR luminosity of the elliptical galaxies increases with L_B but again, we find that the correlation is not statistically significant, with L_B ($\tau = 0.36$ and $P = 91\%$; see footnote 27); the results of the regression analysis produces the following relationship (with $\sigma_r = 0.33$; see footnote 28):

$$\log L_{\rm FIR}({\rm E}) = (1.00 \pm 0.77)\log(L_B) - 2.44. \quad \text{(B3)}$$

The correlations in Equations (B2) and (B3) are plotted in Figure 10. The lack of any strong correlation between $L_{\rm FIR}$ and L_B does not provide any evidence for the hypothesis that the dust responsible for the FIR–submm emission is produced by stellar mass loss, although the ETGs do at least fall in roughly the right place in the figure.

In Figure 10 (lower panel), we also compare the dust mass with optical and X-ray luminosities but find no evidence for a correlation due to the small numbers in the samples with both *Herschel* detections and X-ray fluxes in the literature.

There is also no evidence for a significant correlation between dust mass and L_B for S0 galaxies ($r_S = 0.27$ and $P = 90\%$), with a best-fit relationship ($\sigma_r = 0.58$; see footnote 29):

$$\log M_d({\rm S0}) = (1.11 \pm 0.62)\log L_B - 5.08. \quad \text{(B4)}$$

The dust mass and optical luminosity for the ellipticals are also not correlated ($\tau = 0.30$ and $P = 90\%$[27]), with a best-fit relationship ($\sigma_r = 0.87$; see footnote 28):

$$\log M_d({\rm E}) = (1.89 \pm 1.99)\log L_B - 14.40. \quad \text{(B5)}$$

The remaining panel in Figure 10 shows dust mass rather than FIR luminosity plotted against X-ray luminosity, with both quantities being normalized by L_B; the correlation is weaker when FIR luminosity is converted into dust mass.

REFERENCES

Abazajian, K. N., Adelman-McCarthy, J. K., & Agüeros, M. A. 2009, ApJS, 182, 543
Athey, A., Bregman, J., Bregman, J., Temi, P., & Sauvage, M. 2002, ApJ, 571, 272
Auld, R., Smith, M. W. L., Bendo, G., et al. 2011, MNRAS, in press (arXiv:1109.5706)
Baes, M., Clemens, M., Xilouris, E. M., et al. 2010, A&A, 518, 53
Barlow, M., Krause, O., Swinyard, B. M., et al. 2010, A&A, 518, 138
Becker, R. H., White, R. L., & Helfand, D. J. 1995, ApJ, 450, 559
Bendo, G., Boselli, A., Dariush, A., et al. 2012, MNRAS, 419, 1833
Bendo, G. J., Calzetti, D., Engelbracht, C., et al. 2007, MNRAS, 380, 1313
Bendo, G. J., Galliano, F., & Madden, S. C. 2011, MNRAS, in press (arXiv:1202.4629)

[29] Using the Spearman rho correlation test; this statistic is more appropriate than the Kendall τ used for the ellipticals since the S0s are a larger sample with more detections. The correlation determines how well the relationship between X and Y can be described by a monotonic function. This test is less sensitive to outliers than the similar Pearson correlation test. We tested that the Kendall's τ and Spearman correlation tests give similar values.

Bendo, G. J., Wilson, C. D., Pohlen, M., et al. 2010a, A&A, 518, 65
Bendo, G. J., Wilson, C. D., Warren, B. E., et al. 2010b, MNRAS, 402, 1409
Bendo, G. J., Joseph, R. D., Wells, M., et al. 2003, AJ, 125, 2361
Binggeli, B., Sandage, A., & Tammann, G. 1985, AJ, 90, 1681
Boselli, A., Boissier, S., Heinis, S., et al. 2011, A&A, 528, 107
Boselli, A., Ciesla, L., Buat, V., et al. 2010a, A&A, 518, 61
Boselli, A., Eales, S., Cortese, L., et al. 2010b, PASP, 122, 261
Boselli, A., & Gavazzi, G. 2006, PASP, 118, 517
Bower, G. A., Heckman, T. M., Wilson, A. S., & Richstone, D. O. 1997, ApJ, 483, 33
Bregman, J. N., Snider, B. A., Grego, L., & Cox, C. V. 1998, ApJ, 499, 670
Bressan, A., Panuzzo, P., Buson, L., et al. 2006, ApJ, 639, 55
Brown, B. A., & Bregman, J. N. 1998, ApJ, 495, 75
Capaccioli, M., Caon, N., & D'Onofrio, M. 1992, MNRAS, 259, 323
Cappellari, M., Emsellem, E., Krajnović, D., et al. 2011, MNRAS, 413, 813
Clemens, M., Jones, A. P., Bressan, A., et al. 2010, A&A, 518, 50
Cole, S., Lacey, C., Baugh, C., & Frenk, C. 2000, MNRAS, 319, 168
Combes, F., Young, L. M., & Bureau, M. 2007, MNRAS, 377, 1795
Corbelli, E., Bianchi, S., Cortese, L., et al. 2011, A&A, submitted
Cortese, L., Bendo, G. J., Boselli, A., et al. 2010a, A&A, 518, 63
Cortese, L., Catinella, B., Boissier, S., Boselli, A., & Heinis, S. 2011, MNRAS, 415, 1797
Cortese, L., Ciesla, L., Boselli, A., et al. 2012, A&A, in press (arXiv:1201.2762) (C12)
Cortese, L., Davies, J. I., Pohlen, M., et al. 2010b, A&A, 518, 49
Cortese, L., & Hughes, T. M. 2009, MNRAS, 400, 1225
Crocker, A. F., Bureau, M., Young, L. M., & Combes, F. 2011, MNRAS, 410, 1197
Davies, J. I., Baes, M., Bendo, G. J., et al. 2010, A&A, 518, 48
Davies, J. I., Bianchi, S., Cortese, L., et al. 2012, MNRAS, 419, 3505
Davis, T. A., Alatalo, K., Sarzi, M., et al. 2011, MNRAS, 417, 882
De Lucia, G., Springer, V., White, S., Croton, D., & Kauffmann, G. 2006, MNRAS, 366, 499
Devereux, N., & Eales, S. 1989, ApJ, 340, 708
di Serego Alighieri, S., Gavazzi, G., Giovanardi, C., et al. 2007, A&A, 474, 851
di Serego Alighieri, S., Trinchieri, G., & Brocato, E. 1990, in Windows on Galaxies, ed. G. Fabbiano, J. S. Gallagher, & A. Renzini (Astrophysics and Space Science Library, Vol. 160; Dordrecht: Kluwer), 301
Dowell, C. D., Pohlen, M., Pearson, C., et al. 2010, Proc. SPIE, 7731, 101
Draine, B. T. 2003, ARA&A, 41, 241
Draine, B. T., & Salpeter, E. E. 1979, ApJ, 231, 438
Dressler, A. 1980, ApJ, 236, 351
Dunne, L., Gomez, H. L., Da Cunha, E., et al. 2011, MNRAS, 417, 1510
Eales, S., Dunne, L., Clements, D., et al. 2010, PASP, 122, 499
Emsellem, E., Cappellari, M., Krajnović, D., et al. 2007, MNRAS, 379, 401
Emsellem, E., Cappellari, M., Krajnović, D., et al. 2011, MNRAS, 414, 888
Engelbracht, C. W., Hunt, L. K., Skinna, R. A., et al. 2010, A&A, 518, 56
Faber, S., & Gallagher, J. 1976, ApJ, 204, 365
Feigelson, E. D., & Nelson, P. I. 1985, ApJ, 293, 192
Ferrarese, L., Côté, P., Jordán, A., et al. 2006, ApJS, 164, 334
Ferrari, F., Pastoriza, M. G., Macchetto, F. D., et al. 2002, A&A, 389, 355
Filho, M. E., Barthel, P. D., & Ho, L. C. 2006, A&A, 451, 71
Forbes, D. 1991, MNRAS, 249, 779
Gavazzi, G., & Boselli, A. 1999, A&A, 343, 86
Gavazzi, G., Boselli, A., Donati, A., et al. 2003, A&A, 400, 451
Gavazzi, G., Boselli, A., Scodeggio, M., et al. 1999, MNRAS, 304, 595
Gomez, H. L., Baes, M., Cortese, L., et al. 2010, A&A, 518, 45
Gomez, H. L., Clark, C. J. R., Krause, O., et al. 2012, MNRAS, in press (arXiv:1111.6627)
González-Martín, O., Masegosa, J., Márquez, I., Guainazzi, M., & Jiménez-Bailón, E. 2009, A&A, 506, 1107
Gordon, K. D., Engelbracht, C. W., Fadda, D., et al. 2007, PASP, 119, 1019
Goudfrooij, P., & de Jong, T. 1995, A&A, 298, 784
Goudfrooij, P., Hansen, L., Jorgensen, H. E., et al. 1994, A&AS, 104, 179
Graham, A. W., & Worley, C. C. 2008, MNRAS, 388, 1708
Greggio, L., & Renzini, A. 1990, ApJ, 364, 35
Griffin, M. J., Abergel, A., Abreu, A., et al. 2010, A&A, 518, 3
Griffin, M. J., Swinyard, B., Vigroux, L., et al. 2008, Proc. SPIE, 7010, 80
Haynes, M. P., Giovanelli, R., Martin, A. M., et al. 2011, AJ, 142, 170
Helou, G., Soifer, B., & Rowan-Robinson, M. 1985, ApJ, 298, 7
Ho, L. C., Filippenko, A. V., & Sargent, W. L. W. 1997, ApJS, 112, 315
Jones, C., Forman, W., Vikhlinin, A., et al. 2002, ApJ, 567, 115
Junor, W., Biretta, J. A., & Livio, M. 1999, Nature, 401, 891
Kaneda, H., Onaka, T., & Sakon, I. 2005, ApJ, 632, 83
Kaneda, H., Onaka, T., Sakon, I., et al. 2008, ApJ, 684, 270
Kaviraj, S., Schawinski, K., Devriendt, J. E. G., et al. 2007, ApJS, 173, 619
Kenney, J. D. P., Tal, T., Crowl, H., et al. 2008, ApJ, 687, 69

Kennicutt, R. C., Calzetti, D., Aniano, G., et al. 2011, PASP, 123, 1347
Kennicutt, R. C., Jr, Armus, L., Bendo, G., et al. 2003, PASP, 115, 928
Knapp, R., Guhathakurta, P., Kim, D.-W., & Jura, M. A. 1989, ApJS, 70, 329
Laurikainen, E., Sato, H., Buta, R., & Knapen, J. H. 2010, MNRAS, 405, 1089
Leeuw, L. L., Hawarden, T. G., Matthews, H. E., Robson, E. I., & Eckart, A. 2002, ApJ, 565, L131
Leeuw, L. L., Sansom, A. E., & Robson, E. I. 2000, MNRAS, 311, 683
Li, Y., & van Gorkom, J. H. 2001, in ASP Conf. Ser. 240, in Gas and Galaxy Evolution, ed. J. E. Hibbard, M. Rupen, & J. H. van Gorkom (San Francisco, CA: ASP), 637
Lisenfeld, U., Verdes-Montenegro, L., Sulentic, J., et al. 2007, A&A, 462, 507
Lucero, D. M., & Young, L. M. 2007, AJ, 134, 2148
Martel, A. R., Ford, H. C., Bradley, L. D., et al. 2004, AJ, 128, 2758
Martin, D. C., Fanson, J., Schiminovich, D., et al. 2005, ApJ, 619, 1
Matsuura, M., Dwek, E., Meixner, M., et al. 2011, Science, 333, 1258
Morgan, H. L., & Edmunds, M. G. 2003, MNRAS, 343, 427
Morganti, R., de Zeeuw, P. T., Oosterloo, T. A., et al. 2006, MNRAS, 371, 157
Mundell, C. G., James, P. A., Loiseau, N., Schinnerer, E., & Forbes, D. A. 2004, ApJ, 614, 648
Muñoz-Mateos, J. C., Gil de Paz, A., Boissier, S., et al. 2009, ApJ, 701, 1965
Naab, T., & Ostriker, J. 2009, ApJ, 690, 1452
Nolthenius, R. 1993, ApJS, 85, 1
Noordermeer, E., van der Hulst, J. M., Sancisi, R., Swaters, R. A., & van Albada, T. S. 2005, A&A, 442, 137
Oliver, S. J., Wang, L., Smith, A. J., et al. 2010, A&A, 518, 21
Oosterloo, T., Morganti, R., Crocker, A., et al. 2010, MNRAS, 409, 500
O'Sullivan, E., Forbes, D. A., & Ponman, T. J. 2001, MNRAS, 328, 461
O'Sullivan, E., & Ponman, T. J. 2004, MNRAS, 349, 535
Ott, S. 2010, in ASP Conf. Ser. 434, Astronomical Data Analysis Software and Systems XIX, ed. Y. Mizumoto (San Francisco, CA: ASP), 139
Pahre, M. A., Ashby, M. L. N., Fazio, G. G., & Willner, S. P. 2004, ApJS, 154, 229
Panuzzo, P., Rampazzo, R., Bressan, A., et al. 2011, A&A, 528, 10
Panuzzo, P., Vega, O., Bressan, A., et al. 2007, ApJ, 656, 206
Parkin, T., Wilson, C. D., Foyle, K., et al. 2011, MNRAS, in press (arXiv:1202.5323)
Peebles, P., & Nusser, A. 2010, Nature, 465, 565
Pellegrini, S. 2010, ApJ, 717, 640
Perlman, E. S., Mason, R. E., Packham, C., et al. 2007, ApJ, 663, 808
Pilbratt, G. L., Riedinger, J. R., Passvogel, T., et al. 2010, A&A, 518, 1
Planck Collaboration. 2011, A&A, 536, A16
Poglitsch, A., Waelkens, C., Geis, N., et al. 2010, A&A, 518, 2
Rowan-Robinson, M., Roseboom, I. G., Vaccari, M., et al. 2010, MNRAS, 409, 2
Rowlands, K., Dunne, L., Maddox, S., et al. 2012, MNRAS, 419, 2545
Sage, L. J., Welch, G. A., & Young, L. M. 2007, ApJ, 657, 232
Saintonge, A., Kauffmann, G., Kramer, C., et al. 2011, MNRAS, 415, 32
Sandage, A. 1961, The Hubble Atlas (Washington, DC: Carnegie Institution)
Sarazin, C. L., Irwin, J. A., & Bregman, J. N. 2001, ApJ, 556, 533
Sarzi, M., Shields, J. C., Schawinski, K., et al. 2010, MNRAS, 402, 2187
Sauvage, M., & Thuan, Th. X. 1992, ApJ, 396, 69
Schawinski, K., Kaviraj, S., Khochfar, S., et al. 2007, ApJS, 173, 512
Schmitt, H. R. 2001, AJ, 122, 2243
Schweizer, F., & Seitzer, P. 1992, AJ, 104, 1039
Serra, P., et al. 2009, in Panoramic Radio Astronomy: Wide- field 1–2 GHz Research on Galaxy Evolution, published online at http://pos.sissa.it/cgi-bin/reader/conf.cgi?confid=89, id.56
Shapiro, K. L., Falćon-Barruso, J., van den Ven, G., et al. 2010, MNRAS, 402, 2140
Sil'chenko, O. K., Moiseev, A. V., & Shulga, A. P. 2010, AJ, 140, 1462
Skibba, R. A., Engelbracht, C. W., & Dale, D. 2011, ApJ, 738, 89
Skrutskie, M. F., Cutri, R. M., Stiening, R., et al. 2006, AJ, 131, 1163
Smith, M. W. L., Vlahakis, C., Baes, M., et al. 2010, A&A, 518, 51
Sparks, W. B., Macchetto, F., & Golombek, D. 1989, ApJ, 345, 153
Springob, C. M., Haynes, M. P., Giovanelli, R., & Kent, B. R. 2005, ApJS, 160, 149
Stansberry, J. A., Gordon, K. D., Bhattacharya, B., et al. 2007, PASP, 119, 1038
Swinyard, B. M., Ade, P., Baluteau, J.-P., et al. 2010, A&A, 518, 4
Temi, P., Brighenti, F., & Mathews, W. G. 2007a, ApJ, 660, 1215
Temi, P., Brighenti, F., & Mathews, W. G. 2007b, ApJ, 666, 222
Temi, P., Brighenti, F., Mathews, W. G., & Bregman, J. D. 2004, ApJS, 151, 237
Temi, P., Mathews, W. G., Brighenti, F., & Bregman, J. D. 2003, ApJ, 585, 121
Tran, H. D., Tsvetanov, Z., Ford, H. C., et al. 2001, AJ, 121, 2928
Tsai, J. C., & Mathews, W. G. 1996, ApJ, 468, 571
Tully, R. B. 1988, Nearby Galaxies Catalog (Cambridge: Cambridge Univ. Press), 221
van Dokkum, P. G., & Franx, M. 1995, AJ, 110, 2027
Veron-Cetty, M. P., & Veron, P. 2010, A&A, 518, 10
Verter, F., & Rickard, L. J. 1998, AJ, 115, 745
Vlahakis, C., Eales, S., & Dunne, L. 2007, MNRAS, 379, 1042
Walter, F., Sandstrom, K., Aniano, G., et al. 2011, ApJ, 726, 11
Weinzirl, T., Joghee, S., Khochfar, S., Burkert, A., & Kormendy, J. 2009, ApJ, 696, 411
Wright, G., James, P., Joseph, R., & McLean, I. 1990, Nature, 344, 417
Wrobel, J. M. 1991, AJ, 101, 127
Wrobel, J. M., & Heeschen, D. S. 1988, ApJ, 335, 677
Wyder, T. K., Martin, D. C., Schiminovich, D., et al. 2007, ApJS, 173, 293
Xilouris, E. M., Madden, S. C., Galliano, F., Vigroux, L., & Sauvage, M. 2004, A&A, 416, 41
Yi, S. K., Lee, J., Sheen, Y.-K., et al. 2011, ApJS, 195, 22
Yi, S. K., Yoon, S.-J., Kaviraj, S., et al. 2005, ApJ, 619, 111
Young, J. S., & Scoville, N. 1982, ApJ, 260, 41
Young, L. M., Bendo, G. J., & Lucero, D. M. 2009, AJ, 137, 3053
Young, L. M., Bureau, M., Davis, T. A., et al. 2011, MNRAS, 414, 940
Yun, M. S., Reddy, N. A., & Condon, J. J. 2001, ApJ, 554, 803
Zibetti, S., Charlot, S., & Rix, H.-W. 2009, MNRAS, 400, 1181